ABSTRACT

Title of thesis: STOCHASTIC PROPERTIES OF WIDE FIELD INTEGRATED OPTIC FLOW MEASUREMENTS

Scott Owen, Master of Science, 2009

Thesis directed by: Professor J. Sean Humbert
Aerospace Engineering

Wide Field Integration (WFI) is a biologically inspired method of spatially decomposing optic flow estimates to extract relevant behavioral cues for navigation. In this thesis, a framework is developed that allows the direct application of a Kalman filter to improve the state information extracted from optic flow measurements. In addition, the noise properties of optic flow measurements are characterized, and an architecture to propagate the uncertainty in optic flow measurements to WFI state estimates is formalized. The closed-loop performance of a ground robot maneuvering in a straight tunnel using WFI outputs is then analyzed using three different algorithms to compute optic flow. The performance of the robot is characterized by its ability to track the tunnel centerline, and the accuracy of the WFI state estimates are compared with the true state estimates using a visual motion capture system. Lastly, the Kalman filter is implemented on a ground robot and the modified closed-loop performance is analyzed.

STOCHASTIC PROPERTIES OF WIDE FIELD INTEGRATED OPTIC FLOW MEASUREMENTS

by

Scott R. Owen

Thesis submitted to the Faculty of the Graduate School of the
University of Maryland, College Park in partial fulfillment
of the requirements for the degree of
Master of Science
2009

Advisory Committee:
Prof. J. Sean Humbert
Prof. James E. Hubbard, Jr.
Prof. Rob Sanner

Dedication

I would like to dedicate the work presented in this thesis to my family, for all their support and encouragement over the years. Also, to all the teachers I've had growing up that have pushed me to learn, and become the best student I could become. Thank you all.

Acknowledgments

I would like to acknowledge first and foremost my advisor Sean Humbert for both suggesting this topic and pushing me in the right direction with my work. In addition, I'd like to thank all the grad students in the Autonomous Vehicles Lab for their help over the past two years, especially Andrew Hyslop, Kedar Dimbel, and Bryan Patrick.

Chapter 1

INTRODUCTION

There has been a tremendous rise in interest of autonomous navigation and control for ground, air, and space vehicles over recent years. This demand for autonomy stems largely from the desire to substitute machines for humans in the front lines of the battlefield. Not only does this paradigm shift in war-fighting mitigate human casualties, but it often results in decreased costs, and increased efficiency of intelligence gathering. For instance, in a recent New York Times article, commanders in Iraq and Afghanistan describe their support for drone aircraft by saying that their ability to "linger for up to 22 hours," while "streaming instant video warnings of insurgent activity, has been crucial to reducing threats from roadside bombs and identifying terrorist compounds [6]." However, current autonomous aircraft, and their ground and space counterparts, are limited in the sense that they require a human operator whenever the vehicle encounters a cluttered environment. This limitation introduces potential problems such as latency in pilot commands and communication failures due to weather. To compensate for these misgivings, vision based navigation and control methods can give the vehicle a sense of "self-awareness," in that the vehicle can avoid obstacles independent of any human input. Optic flow, or a mapping of the local velocity field relative to the vehicle, has previously been shown to be an effective sensory mechanism for such a purpose[14],[22],

[13], and [21]. In this regards, not only is it important to estimate optic flow efficiently, but a control methodology must be established that allows one to implement this information in a meaningful way; it is for this reason that the sensory mechanisms developed to in the insect visuomotor system are able to yield such valuable insight into autonomous navigation of man made vehicles.

It has been shown through both neurological and physiological evidence, as well as response heuristics observed in insect flight movement [27], that global optic flow estimates are the sensory inputs insects require to avoid obstacles, and adjust airspeed in cluttered environments [13]. Furthermore, it has been observed that insects make local optic flow estimates, and compare the corresponding global flow map to preferred patterns that have developed phylogenetically using specialized neurons called tangential cells [7]. The response of these cells to the observed estimated optic flow field contains information regarding the relative position of the insect to its surroundings, and in turn triggers motor commands in the wing muscles to respond accordingly. The extraction of information for navigational purposes based on the spatial decomposition of optic flow in the visuomotor system is referred to as Wide Field Integration (WFI), and was modeled in [13]. It was shown that when the optic flow estimates are spatially decomposed against known basis functions, behaviorally relevant information such as speed and position relative to the surrounding obstacles can be extracted.

The visuomotor system of an insect can provide between several hundred and several thousand localized optic flow estimates [7]. In this respect, although the sensory neurons in the insect visuomotor system are unsophisticated and provide

relatively noisy estimates, the global flow field is robust to these localized variations. On man-made platforms, however, optic flow can be computed in several ways, and these algorithms range from unsophisticated models that provide patterns similar to those observed in the insect visuomotor system, to highly sophisticated algorithms that implement advanced iterative optimization schemes. An extensive overview of these algorithms is presented in [1] and [30], while [22] and [15] compare the effectiveness of these algorithms in providing tunnel centering and obstacle avoidance. Due to the large number of pixels involved, and the high frame rate required for control, any dynamic filtering strategy with the purpose of improving optic flow estimates is bound to be computationally intensive, and thus would not lend itself to application on MAVs. In contemporary work, researchers who have applied a dynamic filtering stagey with respect to optic flow have done so to either clean up background noise in the imagery [29], or use it in conjuncture with additional sensors, such as an IMU, to yield inertial state estimates of a vehicle [**?**]. However, in this thesis, a method is proposed of using the behaviorally relevant information extracted from the optic flow estimates using WFI techniques.

For this purpose, the stochastic properties of the optic flow estimates, and how these characteristics relate to relative state estimates are investigated both theoretically, and experimentally. First, a method is derived to propagate uncertainty in the optic flow estimates to uncertainty in the relative state estimates; and second, a framework is developed so that the WFI outputs can be used by a discrete Kalman filter [17] to [5] reduce the noise in these estimates. The experimental results first build on the work of [28], and describe the noise characteristics of the optic flow as

a function of the image contrast, background lighting and turn-rate. Three different algorithms are then used to compute optic flow, and are implemented on a ground robot to demonstrate closed loop control, as well as to quantify the performance of each method. The algorithms tested are the Neuromorphic Elementary Motion Detector [27], a 1-D Gradient-Method [29] [12] and [18], and a Pyramid Iterative Lucas-Kanade algorithm [20] and [2]. The performance of each algorithm is evaluated with respect to the RMS error and the mutual information between the true position - determined using a Vicon motion capture system - and the estimated position, as well as the ability of the ground robot to track the centerline of a tunnel. Lastly, a discrete Kalman filter is implemented on a ground robot using optic flow estimates from the gradient method and Lucas-Kanade algorithm to generate state information, and a preliminary investigation into its effectiveness is presented.

Chapter 2

Optic Flow Description and State Estimation

Optic flow is a measurement of relative motion, and may be computed in real time based on the extraction of spatial and temporal information from successive images taken from an onboard camera. Optic flow constrained to three degrees of freedom in the horizontal plane is a function restricted to $L_2[0, 2\pi]$ in the viewing angle γ [14]:

$$\dot{Q}(\gamma, \mathbf{x}) \;=\; -\dot{\theta} + \mu(\gamma, \mathbf{x})(\dot{x}_b \sin\gamma - \dot{y}_b \cos\gamma), \tag{2.1}$$

where the vehicle's state is given as $\mathbf{x} = (y, \theta)$, and μ is the nearness function defined as the reciporical of the distance of the vehicle to the nearest object at a viewing angle γ (Figure 2.1).

The nearness function is determined based on the distribution and location of objects relative to the vehicle. A practical nearness function corresponds to a straight tunnel environment, and it is illustrated in Figure 2.1. For a vehicle in a straight tunnel, the nearness function is given by:

$$\mu(\gamma, \mathbf{x}) \;=\; \begin{cases} \frac{\sin(\gamma+\theta)}{a-y} & 0 \le \gamma + \theta < \pi \\ -\frac{\sin(\gamma+\theta)}{a+y} & \pi \le \gamma + \theta < 2\pi \end{cases} \tag{2.2}$$

In Section 5 the stochastic properties of the optic flow estimates will be analyzed by rotating a ground robot in a cylindrical test section. In this environment, (2.1)

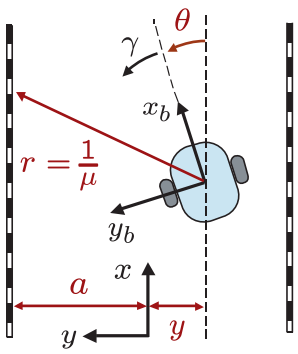

Figure 2.1: Planar tunnel geometry - notation and vehicle state definitions

simplifies to

$$\dot{Q}(t) = -\dot{\theta}(t). \tag{2.3}$$

2.1 Optic Flow Algorithms

In this section, the three optic algorithms that will be implemented on the ground robot are reviewed. These algorithms include the 1-D Gradient Method (GM), the 2-D Pyramid Iterative Lucas-Kanade (LK), and the Neuromorphic Elementary Motion Detector (NE).

The GM relies on estimating optic flow based on the assumption that the intensity of an image is conserved between successive frames. In its most primative form (and as applied experimentally in this thesis) the optic flow estimate is derived based on a first order multivariate Taylor Series expansion of the image intensity:

$$I(x_o, t_o) = I_o, \tag{2.4}$$

$$I(x_o + \Delta x, t_o + \Delta t) = I_o + \frac{\partial I}{\partial x}dx + \frac{\partial I}{\partial t}dt. \tag{2.5}$$

Thus, since (2.4) equals (2.5) under the assumption that image intensity is conserved,

$$\frac{\partial I}{\partial x}dx + \frac{\partial I}{\partial t}dt = 0. \tag{2.6}$$

Dividing through by the change in time and solving for dx/dt yields

$$\frac{dx}{dt} = \frac{-\partial I/\partial t}{\partial I/\partial x}. \tag{2.7}$$

In implementation, the luminance values of the individual pixels are first de-sampled by taking an unweighted average over a window of neighboring pixels, and then optic flow is computed using each of these *metapixels*. Doing so increases the maximum shift estimate between frames the algorithm can calculate. The flow estimates are then de-sampled to around 20 or 40 by taking an unweighted average of adjacent metapixels. These new averages are referred to as *cells*, and are then de-sampled again by averaging 4 different rows. An outlier rejection criteria to discard unreasonably large optic flow has also proven helpful.

The LK algorithm is a modified GM that is much more robust to larger pixel shifts between frames, and - as implemented in *OpenCV* software - generalizes this flow estimate to 2-D. The LK algorithm is more effective in estimating the optic flow than the GM for two essential reasons. First, it takes advantage of a Newton-Raphson iterating optimization scheme, based on minimizing the square difference of the image intensity between frames over a given window (w_x, w_y) of pixels. That is, given that **u** and **v** are two distinct locations in the (x,y) plane - such that $I_1(u_x, u_y)$ and $I_2(v_x, v_y)$ correspond to successive frames in the image sequence - and that the location of interest **v** in the second frame can be defined in terms of **u** from

the first frame, as well as the the optic flow estimate between frames, $\mathbf{v} = \mathbf{u} + \dot{\mathbf{Q}}\Delta T$, then a cost function can be defined based on the L_2 norm of the two images:

$$J(\dot{\mathbf{Q}}) = \sum_{x=u_x-w_x}^{u_x+w_x} \sum_{y=v_x-w_y}^{v_x+w_y} \Big[I_1(u_x, u_y) - I_2(u_x + \dot{Q}(x,t)\Delta T, u_y + \dot{Q}(y,t)\Delta T \Big]^2. \quad (2.8)$$

If we have (or guess) an initial estimate of the optic flow, $\dot{\mathbf{Q}}_o$, and assume that the true optic flow can be defined as $\dot{\mathbf{Q}} = \dot{\mathbf{Q}}_o + \Delta\dot{\mathbf{Q}}$, then the Newton-Raphson algorithm iteratively minimizes this cost function until either the value of $\Delta\dot{\mathbf{Q}}$ does not change significantly between iterations, or a maximum preset number of iterations is reached. The second reason this algorithm is more effective than the GM in estimating the true optic flow is because the LK algorithm repeats the Newton-Raphson optimization at sequentially more resolute versions of the images. Doing so helps assure that the estimate, $\dot{\mathbf{Q}}_o$, is in the vicinity of the true value, and thus the optimization reaches a global minima, opposed to a local minima or even diverging. A more detailed discussion on taking this derivative and solving for the optimal optic flow estimate is given in [2]. Elementary Motion Detector (EMD) algorithms

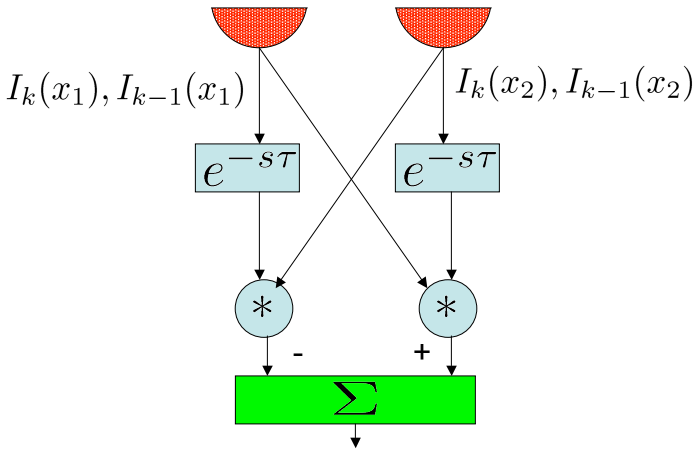

Figure 2.2: Elementary Motion Detector block diagram.

- in their most primitive form - are unsophisticated, and yield very noisy optic flow estimates similar to the patterns observed in the compound retina of an insect [27]. They compute optic flow from correlating image intensities between either neigborhood, or second neighborhood pixels after spatiotemporal filters are applied[Santen]. The correlation process is illustrated in Figure 2.2, and defined in (2.9):

$$\dot{Q}(x,t) = I_1(x_1)I_2(x_2) - I_1(x_2)I_2(x_1). \tag{2.9}$$

The Neuromorphic EMD modifies 2.9, by approximating additional subtleties in the insect visuometer system. These additions include a saturating nonlinearity to model threshold limits of various insect neurons, various low and high pass filters to reduce noise, and a contrast gain control to model *motion adaptation*. Motion adaptation is a phenomenon in which the response of tangential cells to external stimuli decreases with continual excitation. One additional benefit of the NE algorithm is that it can be implemented on analogue circuitry. A complete description of the NE, and its circuitry is presented in [27].

2.2 Uncertainty in Optic Flow Estimates

Optic flow estimates are corrupted by several sources of noise, and the combined effect of these uncertainties have been modeled in [28] [18] and [29] as being zero mean, additive white Gaussian noise. That is,

$$\dot{\tilde{Q}}(t,\gamma) \;=\; \dot{Q}(t,\gamma) + \nu(t,\gamma), \tag{2.10}$$

where $\dot{\tilde{Q}}(t,\gamma)$ is the optic flow measurement, and ν is assumed to be zero mean, white, and uncorrelated with itself at different viewing angles.

$$E[\nu(t,\gamma)] = 0 \tag{2.11}$$

$$E[\nu(t_1,\gamma)(\nu(t_2,\gamma)] = R\delta(t-\tau) \tag{2.12}$$

These characteristic assumptions of the optic flow noise are evaluated in Section 5; however, in this section, potential sources of the noise are reviewed.

Noise in optic flow estimates arise from hardware constraints, the image processing routine, and limitations of the algorithms used to compute optic flow. The uncertainty in optic flow estimates introduced by hardware constraints are related to resolution, frame rate, processor speed (and/or memory allocation), and structural vibrations. It is shown in [18] that when using the GM the sampling error for the spatial gradient is directly proportional to the camera resolution, while the sampling error for the temporal gradient is directly proportional to the frame rate. On a related note, if the resolution of the image is too fine, the algorithm can give unrealistic predictions because of possible high spatial frequency content. For this reason, [29] suggests pre-blurring the image using a Gaussian blurring function. The high spatial frequency content can also introduce noise in the form of aliasing if the displacements being measured are greater than half a cycle of the highest spatial frequency present in the pre-filtered image sequence [28]. On the other hand, an image with spatial frequency content that is too low potentially does not have enough information to estimate optic flow accurately. The processor speed and memory size can also impact the optic flow estimates. If the computer is overburdened, then

occasionally the optic flow estimates will loose accuracy as a result of the frame rate momentarily decreasing. The decrease in frame rate results in greater shifts between frames, and this shift may be too great for the algorithm to estimate. This phenomenon was noticed in the spin tests while in addition to running the computationally intensive LK algorithm, the computer was also saving imagery at every control interval (20 Hz). This last effect is an important consideration when implementing these algorithms on micro vehicles because they are often performing several tasks with only a limited amount of processing power. Finally, as the sensors are implemented on a vehicle, vibrations can induce oscillations of the mirror relative to the camera.

Noise is also introduced into the optic flow estimates during the image processing routine. This noise is random, and results from digitalizing the vehicles surroundings into pixels with intensity values $I(x, y, t) \in (0, 255)$ [18]. Additional noise can be introduced from distorting the image from a ring of pixels around the mirror, to a row of pixels.

Lastly, uncertainty is introduced as a result of the individual algorithms. For instance, the gradient method relies on taking finite differences to determine the gradients of the image intensity in time and space; taking these derivatives adds random noise. In addition, the gradient method is based on only a first order Taylor Series approximation. Discarding the higher order intensity gradients causes additional error. Thus the accuracy of the optic flow estimates are constrained on the lower end by not having enough information, and on the upper end by having either too much detail, or large unmodeled large second intensity gradients. Lastly,

the gradient method discussed above relies on the assumption that the overall image intensity is conserved throughout the sequence of images; however, this assumption will certainly be violated outside a laboratory without including an adaptive filter sensitive to varying mean luminance values.

On the other hand, the NE algorithm - contrary to the GM - attempts to model the complex processes that occur in the insect visuomotor with contrast gain adjustments, and a series of filters [27]. Therefore, uncertainty in the optic flow estimates can be introduced if any of the filter parameters are poorly chosen. In addition, the NE is designed to correlated luminance values by comparing the intensity estimates of adjacent metapixels. Thus, if a shift in the pixel location between frames is large compared to the size of the metapixel, then the algorithm will give an inaccurate estimate. It is possible to change the algorithm so that it compares intensity values with the second most adjacent metapixel, however, then shifts below 2 metapixels are undetectable.

2.3 Wide-Field Integration

WFI is a method of information extraction modeled on the spatial decomposition of specialized interneurons in the insect visuomotor system [14]. Mathematically, it can be modeled as a spatial inner product that is an abstraction of the "angle" between the pattern and the pre-defined basis function. If we perform this inner product between the optic flow function and some pre-defined basis function, we obtain the projection of the optic flow onto the basis function:

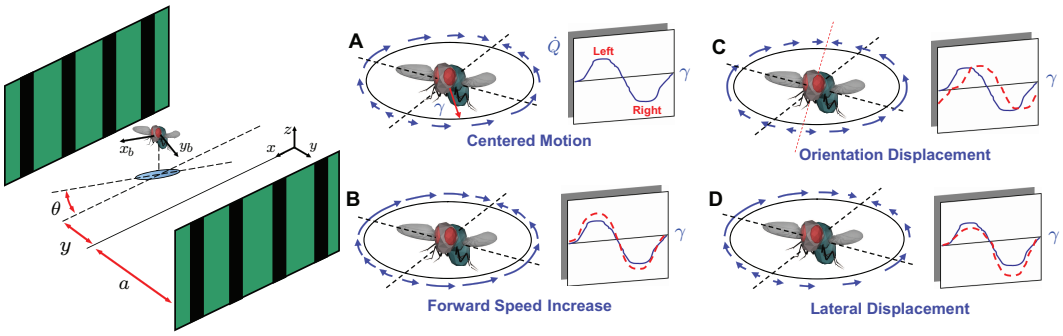

Figure 2.3: Spatial decompositions of optic flow. Amplitude, phase, and asymmetry of the azimuthal optic flow pattern encode relative proximity and speed with respect to obstacles in the environment.

$$\phi_i(t) \quad = \quad \frac{1}{\pi} \int_0^{2\pi} \dot{Q}(\gamma, t) \cdot F_i(\gamma) \, d\gamma. \tag{2.13}$$

By selecting the basis functions carefully, the state information that is embedded in the optic flow function (2.1) may be extracted. In [14] it was shown that when the orthogonal basis set of Fourier harmonics are used to decompose the optic flow, good estimates of the states may be determined; moreover, only the first two harmonics ($F_{a_0} = \frac{1}{\sqrt{2}}$, $F_{a_1} = \cos\gamma$, $F_{a_2} = \cos 2\gamma$, $F_{b_1} = \sin\gamma$, $F_{b_2} = \sin 2\gamma$) are needed to extract all the states. The WFI outputs are generally non-linear, but by linearizing about a nominal trajectory, and assuming a small perturbation model, the primary components of the outputs may be determined. Furthermore, under the assumption that the vehicle is a ground robot maneuvering with zero side slip ($\dot{y}_b = 0$), that it has velocity and turn rate control, and that its nominal trajectory is about the tunnel centerline at a constant speed ($\dot{x}_b = V_0$), then Table 2.1 gives the expected

Mode	Projection $y_j(\boldsymbol{x})$	Linearization $z_j(\boldsymbol{x})$
a_0	$-\sqrt{2}\dot{\theta} + \frac{y}{\sqrt{2}(a^2-y^2)}\ \dot{x}_b \cos\theta$	$-\sqrt{2}\dot{\theta} + \frac{v_0}{\sqrt{2}a^2}\ y$
a_1	$\frac{4a}{3\pi(a^2-y^2)}\ \dot{x}_b \sin\theta\cos\theta$	$\frac{4v_0}{3\pi a}\ \theta$
b_1	$\frac{4a}{3\pi(a^2-y^2)}\ \dot{x}_b(\cos^2\theta + 1)$	$\frac{8}{3\pi a}\ \dot{x}_b$
a_2	$-\frac{y}{2(a^2-y^2)}\ \dot{x}_b \cos\theta$	$-\frac{v_0}{2a^2}\ y$
b_2	$\frac{y}{2(a^2-y^2)}\ \dot{x}_b \sin\theta$	0

Table 2.1: Spatial Fourier decomposition of planar tunnel optic flow for vehicles with sideslip constraint

Fourier coefficients.[1] These results can be inferred from Figure 2.3, which illustrates a fly traversing a straight tunnel. If the fly is in the center of the tunnel and traveling parallel to the walls, then the optic flow on both sides are equal and opposite in magnitude, while the optic flow forward and aft is zero. If, however, the fly rotates, or moves away from the centerline, the optic flow will be perturbed, and result in either a non-zero a_1 or a_2 Fourier coefficient.

A feedback control methodology has been developed [14],[13], and [15] that uses these perturbations from a desired optic flow pattern to provide a proportional gain feedback controller to regulate the a_1 and a_2 Fourier coefficients, and thus the

[1]When $F_i(\gamma)$ is a general function, then $\phi(t)$ will be referred to the WFI output. In the special case when $F_i = cos(n\gamma), sin(n\gamma)$, then $\phi_i(t)$ is formally referred to as a Fourier coefficient.

perturbation states. Therefore,

$$u = -K_1 a_1 - K_2 a_2, \tag{2.14}$$

where in [13], it was shown that for appropriately chosen gains, the resulting closed loop system is asymptotic stable. In [16], these results are extended to 6-DOF motion in a 3-D environment, and obstacle avoidance of a simulated aircraft is demonstrated.

Chapter 3

Ground Robot Dynamic Model

3.1 Continuous Time Model

In [14] [13] [15], a ground robot was used as a test platform to implement the optic flow and WFI algorithms. The ground robot has nonlinear dynamics

$$\begin{aligned} \dot{x} &= V\cos\theta \\ \dot{y} &= V\sin\theta \\ \dot{V} &= u_1 \\ \dot{\theta} &= u_2, \end{aligned} \tag{3.1}$$

where $V = \dot{x}_b$ is the vehicle's forward speed, u_1 controls the forward speed of the vehicle, and u_2 is the rotation rate of the vehicle. For obstacle avoidance and tunnel centering applications, u_2 is fixed by an inner loop controller, and u_1 commands a differential rotation rate in each of the two wheels. Furthermore, if the system is linearized about the reference trajectory $(y, \theta) = (0, 0)$ and a constant forward speed $V = V_0$, then the forward speed dynamics decouple from the (y, θ) dynamics. The resulting (y, θ) dynamics are given by

$$\frac{d}{dt}\begin{pmatrix} y \\ \theta \end{pmatrix} = \begin{pmatrix} 0 & V_0 \\ 0 & 0 \end{pmatrix}\begin{pmatrix} y \\ \theta \end{pmatrix} + \begin{pmatrix} 0 \\ 1 \end{pmatrix}\dot{\theta} + \mathbf{d}. \tag{3.2}$$

The control input in this paper is modeled as a deterministic signal; however, for the eventual application to a Kalman filter, the stochastic input $\mathbf{d}$ is included as fictitious, low amplitude, zero mean white Gaussian noise. Doing so helps ensure that the error covariance matrix used in the Kalman filter algorithm remains positive definite [3] [8]. That is,

$$\begin{aligned} E[\mathbf{d}] &= 0 \\ E[\mathbf{d}\mathbf{d}^T] &= D\delta(t-\tau). \end{aligned} \tag{3.3}$$

The output equations incorporate the results from the linearizations given in Table 2.1; therefore,

$$\begin{pmatrix} y \\ \theta \end{pmatrix} = \begin{pmatrix} 0 & \frac{-2a^2}{V_0^2} \\ \frac{3\pi a}{4V_0} & 0 \end{pmatrix} \begin{pmatrix} a_1 \\ a_2 \end{pmatrix} + \mathbf{n}, \tag{3.4}$$

where $\mathbf{n}$ represents measurement noise. However, it can be useful to represent the dynamics in terms of the Fourier coefficients. A change of variables with $\boldsymbol{\phi} = P^{-1}\mathbf{x}$ and dynamics $\dot{\mathbf{x}} = A\mathbf{x} + Bu$, where $\boldsymbol{\phi} = [a_2, a_1]^T$, leads to the relation:

$$\frac{d}{dt}(\boldsymbol{\phi}) = PAP^{-1}\boldsymbol{\phi} + PBu. \tag{3.5}$$

Therefore, the modified dynamics are found to be:

$$\frac{d}{dt}\begin{pmatrix} a_2 \\ a_1 \end{pmatrix} = \begin{pmatrix} 0 & \frac{3\pi V_0}{8a} \\ 0 & 0 \end{pmatrix} \begin{pmatrix} a_2 \\ a_1 \end{pmatrix} + \begin{pmatrix} 0 \\ \frac{4V_0}{3\pi a} \end{pmatrix} \dot{\theta} + \mathbf{d}. \tag{3.6}$$

3.2 Discrete Time Model

The dynamics of the ground robot are continuous; however, the measurements of the Fourier coefficients are discrete. For this reason, the system dynamics must

be discretized in order to implement a Kalman filter. The discrete model equivalent to (3.2) is

$$\mathbf{x}_{k+1} = F\mathbf{x}_k + G\mathbf{u}_k + \mathbf{w}_k \tag{3.7}$$

$$\mathbf{y}_k = H\mathbf{x}_k + \mathbf{n}_k, \tag{3.8}$$

where F, G, and H are constant matrices, and

$$E[\mathbf{w}_k] = E[\mathbf{n}_k] = 0. \tag{3.9}$$

In addition, the second order statistics are given by

$$E[\mathbf{w}_k\mathbf{w}_r^T] = W\delta_{rk} \tag{3.10}$$

$$E[\mathbf{n}_k\mathbf{n}_r^T] = R_{nn} \tag{3.11}$$

$$E[\mathbf{w}_k\mathbf{n}_r^T] = 0. \tag{3.12}$$

As previously discussed, the variance of the input disturbance is assumed to be zero mean white-Gaussian noise, while the measurement noise is only assumed to be zero mean. For a linear time invariant system with a uniform sampling period ΔT, and a disturbance noise modeled as Wide Sense Stationary (WSS) and white, the Van Loan algorithm can be used to discretize the system [23]. Although the details of this method are not discussed, the desired matrices can be computed using

$$\Lambda = \begin{pmatrix} -A & BWB^T \\ 0_{n\times n} & A^T \end{pmatrix}, \tag{3.13}$$

where A and B are defined in (3.6). Thus the necessary parameters for (3.7) can be

found by computing $M = e^{\Lambda \Delta T}$,

$$M = \begin{pmatrix} M_{11} & F^{-1}W \\ 0_{n\times n} & F^T \end{pmatrix}, \tag{3.14}$$

and,

$$G = \left[\int_0^{\Delta T} e^{A\sigma}\, d\sigma\right] B \tag{3.15}$$

Chapter 4

Theoretical Framework for State Measurement Noise

It was previously stated that the WFI outputs used for closed loop control vary depending on the specific application, as well as the environment that the vehicle is operating in. Thus, it is most practical to model the stochastic properties of the optic flow estimates and have a general method to propagate the resulting noise model to the desired state estimates. The results derived in this section provide this framework, and Figure 4.1 summarizes the process.

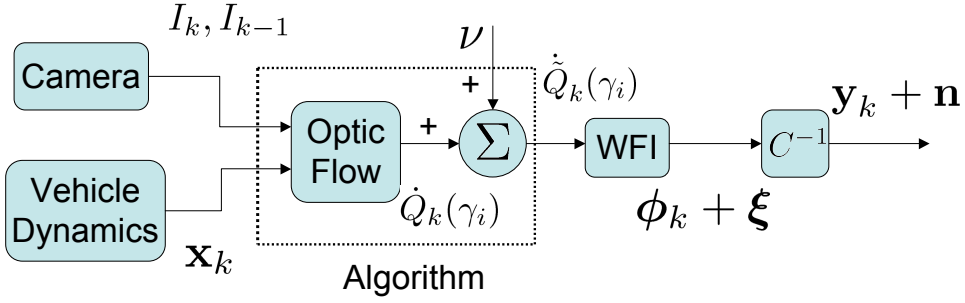

Figure 4.1: Expansion of the plant dynamics and sensing block, as it would appear in a standard unity feedback block diagram.

4.1 Propagating Optic Flow Estimates

In this section, a model representing the second order statistics of the WFI outputs are derived based on the noise properties of the optic flow. If it is assumed that the estimated optic flow in a given row of pixels can be represented as a linear

combination of deterministic optic flow and additive noise, then

$$\dot{\tilde{Q}}(t,\gamma) \;=\; \dot{Q}(t,\gamma) + \nu(t,\gamma), \tag{4.1}$$

where $\dot{\tilde{Q}}(t,\gamma)$ represents the estimated optic flow, and ν is assumed to be zero mean with a known covariance:

$$E[\nu(t,\gamma)] \;=\; 0 \tag{4.2}$$

$$E[\nu(t_1,\gamma)(\nu(t_2,\gamma)] \;=\; R_{vv}(t_1,t_2,\gamma). \tag{4.3}$$

A general framework of the noise will be developed, and thus the second order statistics of the optic flow estimates will remain arbitrary with assumptions being added as necessary to reduce the complexity of the model. First, it is assumed that the noise can be modeled as a Wide Sense Stationary process (WSS) and uncorrelated with it self at different viewing angles, then (4.3) may be simplified. The assumption that the noise is uncorrelated at different viewing angles will be analyzed in Section 5; however, as discussed in [29] any effects resulting in this correlation have been observed to be minimal.[1] Thus,

$$E[\nu(t_1,\gamma)(\nu(t_2,\gamma)] \;=\; R_{vv}(\tau), \tag{4.4}$$

where $\tau = t_2 - t_1$. The decomposition of the optic flow pattern with various basis functions F_i, as previously mentioned, allows one to extract information about the state variables, assuming F_i is chosen appropriately. If the definition of the WFI

[1] Singh's discussion on this topic is in reference to estimating optic flow using correlation based methods, which rely on a probabilistic description of the optic flow over a given neighborhood of pixels.

outputs (2.13) is modified to include the noise model just discussed, then over an arbitrary interval $[\Gamma_1, \Gamma_2] \subset [0, 2\pi]$,

$$\begin{aligned}
\tilde{\phi}_1(t) &= \frac{1}{\pi}\int_{\Gamma_1}^{\Gamma_2} F_1(\gamma)\left\{\dot{Q}(t,\gamma)+\nu(t,\gamma)\right\}d\gamma \\
\tilde{\phi}_2(t) &= \frac{1}{\pi}\int_{\Gamma_1}^{\Gamma_2} F_2(\gamma)\left\{\dot{Q}(t,\gamma)+\nu(t,\gamma)\right\}d\gamma \\
&\vdots \\
\tilde{\phi}_m(t) &= \frac{1}{\pi}\int_{\Gamma_1}^{\Gamma_2} F_m(\gamma)\left\{\dot{Q}(t,\gamma)+\nu(t,\gamma)\right\}d\gamma. \qquad (4.5)
\end{aligned}$$

Thus, the nonlinear observer model,

$$\tilde{\mathbf{y}} = h(\mathbf{x}) + \boldsymbol{\nu}, \qquad (4.6)$$

in the WFI framework is given as:

$$\tilde{\boldsymbol{\phi}}(t) = \frac{1}{\pi}\int_{\Gamma_1}^{\Gamma_2} \mathbf{F}(\gamma)\left\{\dot{Q}(t,\gamma)+\nu(t,\gamma)\right\}d\gamma. \qquad (4.7)$$

Since in practice we do not have access to the optic flow measurements at every instance in time, more insight can be obtained by discretizing (4.7) in space and time. Doing so based on a midpoint Riemann sum approximation yields

$$\begin{aligned}
\tilde{\boldsymbol{\phi}}_k &= \frac{1}{\pi}\sum_{i=1}^{n} \mathbf{F}(\gamma_i)\left\{\dot{Q}_k(\gamma_i)+\nu_k(\gamma_i)\right\}\Delta\gamma \qquad (4.8) \\
&= \frac{1}{\pi}\sum_{i=1}^{n} \mathbf{F}(\gamma_i)\dot{Q}_k(\gamma_i)\Delta\gamma + \frac{1}{\pi}\sum_{i=1}^{n} \mathbf{F}(\gamma_i)\nu_k(\gamma_i)\Delta\gamma, \qquad (4.9)
\end{aligned}$$

where $t = k\Delta T$, and i corresponds to a specific viewing angle (i.e. cell). Thus, the noise model for the WFI outputs are described in terms of the noise model for the optic flow. If (4.9) is re-expressed in short hand as the combination of a deterministic signal and additive noise, similar to the optic flow expression, then

$$\tilde{\boldsymbol{\phi}}_k = \boldsymbol{\phi}_k + \boldsymbol{\xi}, \qquad (4.10)$$

where,

$$E[\boldsymbol{\xi}] = 0 \tag{4.11}$$

$$\begin{aligned} E[\boldsymbol{\xi}_k\boldsymbol{\xi}_r^T] &= E[\{\frac{1}{\pi}\sum_{i=1}^{n}\mathbf{F}(\gamma_i)\nu_k(\gamma_i)\Delta\gamma]\}\{\frac{1}{\pi}\sum_{i=1}^{n}\mathbf{F}(\gamma_i)\nu_r(\gamma_i)\Delta\gamma]\}^T] \\ &= \left(\frac{\Delta\gamma}{\pi}\right)^2 E[\{\sum_{i=1}^{n}\mathbf{F}(\gamma_i)\nu_k(\gamma_i)\}\{\sum_{i=1}^{n}\mathbf{F}(\gamma_i)\nu_r(\gamma_i)\}^T]. \end{aligned} \tag{4.12}$$

Expanding the expectation in (4.12) yields,

$$\begin{aligned} E[\cdot] = \mathbf{F}(\gamma_1)\mathbf{F}^T(\gamma_1)E[\nu_k(\gamma_1)\nu_r(\gamma_1)] + \mathbf{F}(\gamma_1)\mathbf{F}^T(\gamma_2)E[\nu_k(\gamma_1)\nu_r(\gamma_2)] + \cdots \\ +\mathbf{F}(\gamma_1)\mathbf{F}^T(\gamma_n)E[\nu_k(\gamma_1)\nu_r(\gamma_n)] + \cdots + \mathbf{F}(\gamma_n)\mathbf{F}^T(\gamma_n)E[\nu_k(\gamma_n)\nu_r(\gamma_n)]. \end{aligned} \tag{4.13}$$

Under the previous assumption that the noise in the optic flow estimates are constant and uncorrelated with themselves at different viewing angles, the only terms remaining in (4.13) are the terms that have like indices on γ. Thus, (4.12) can be re-written as

$$\begin{aligned} E[\boldsymbol{\xi}_k\boldsymbol{\xi}_r^T] &= \left(\frac{\Delta\gamma}{\pi}\right)^2 R_{\nu\nu}\sum_{i=1}^{n}\mathbf{F}(\gamma_i)\mathbf{F}^T(\gamma_i) \\ &= \frac{\Delta\gamma R_{\nu\nu}}{\pi}\left(\frac{1}{\pi}\sum_{i=1}^{n}\mathbf{F}(\gamma_i)\mathbf{F}^T(\gamma_i)\Delta\gamma\right), \end{aligned} \tag{4.14}$$

for any r, k. This result has the implication that doubling the number of optic flow sample points (cells), decreases $E[\boldsymbol{\xi}_k\boldsymbol{\xi}_r^T]$ by a factor of two. The continuous time theoretical result may be determined by taking the limit as the number of cells approaches infinity:

$$E[\boldsymbol{\xi}(t)\boldsymbol{\xi}^T(t-\tau)] = \lim_{\Delta\gamma\to 0} E[\boldsymbol{\xi}_k\boldsymbol{\xi}_r^T] \tag{4.15}$$

$$= \lim_{\Delta\gamma\to 0}\frac{\Delta\gamma R_{\nu\nu}(\tau)}{\pi}\left(\frac{1}{\pi}\int_{\Gamma_1}^{\Gamma_2}\mathbf{F}(\gamma)\mathbf{F}^T(\gamma)d\gamma\right) \tag{4.16}$$

$$= 0. \tag{4.17}$$

Thus, for any basis function $F_i(\gamma)$ in $L_2[0, 2\pi]$, the projected covariance of the associated WFI outputs approaches zero as the number of optic flow samples approach infinity. This result provides additional support for the usefulness of WFI methods, as it shows that the more optic flow samples used in the integration, the less noisy the resulting Fourier coefficients will be. The result for the discrete case (4.14) is validated using MATLAB in Figure 4.2 for a trivial example involving a constant optic flow signal corrupted by Gaussian noise $\nu(t, \gamma) \sim N(0, 1)$. The agreement the plots have with the theoretical results derived suggests that the assumption that $E[\nu_k(\gamma_i)\nu_r(\gamma_j)] = 0$ is valid.

The previous derivations analyze only the statistics of the optic flow measurements in one row of the image plane. Since the optic flow estimate for each pixel is described by a stochastic process $\{Q(t, \gamma)\}$, the optic flow estimates for each ring at a given γ can be considered an element of the ensemble only if the algorithm used to estimate the optic flow is highly robust to localized variations in contrast levels, or background lighting. Unfortunately optic flow algorithms are highly sensitive to these fluctuations, and thus averaging several rings is necessary to suppress any spurious data points that may result for either of the reasons just mentioned. Furthermore, since $\dot{Q}(t, \gamma)$ represents an unweighted average of the optic flow estimates of each pixel in the image plane within the viewing angle γ, as $\Delta\gamma$ decreases, the optic flow estimates become more vulnerable to the optic flow errors that result from high spatial frequency content in the image.

Finally, to complete the propagation of the noisy optic flow estimates so that they are in a form applicable to (3.8), the nonlinear equations relating the WFI out-

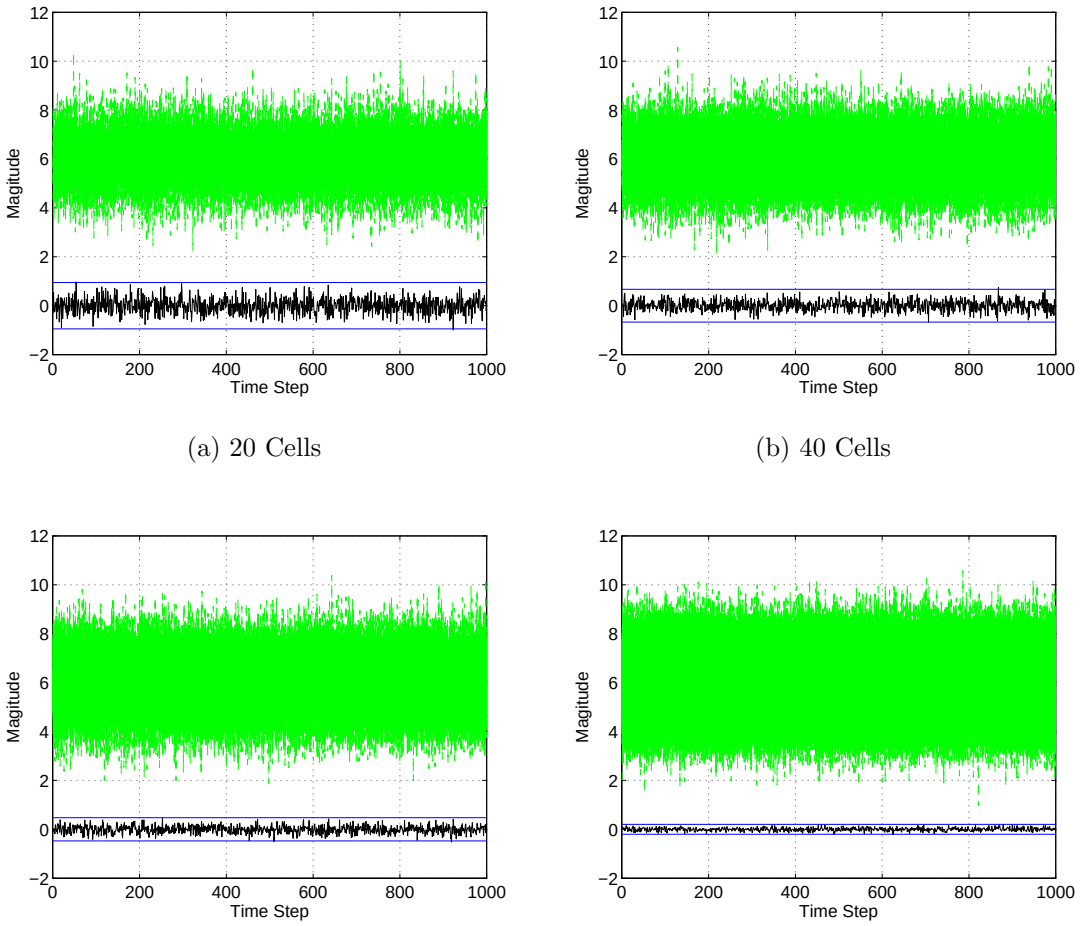

(a) 20 Cells

(b) 40 Cells

(c) 80 Cells

(d) 440 Cells

Figure 4.2: $E[\xi_k \xi_r]$ for a_1 Fourier coefficient (dark) based on noisy optic flow estimates (light). The horizontal lines represent a 3σ confidence interval based on (4.14).

puts to the states are linearized about a reference trajectory, and the corresponding mapping $C \in \mathbb{R}^{n \times n} : \mathbf{y}(\mathbf{t}) \rightarrow \boldsymbol{\phi}(t)$ can be inverted so that

$$\mathbf{y} = C^{-1} \left(\boldsymbol{\phi}(t) + \boldsymbol{\xi} \right). \tag{4.18}$$

Therefore,

$$E[\mathbf{n}(t)\mathbf{n}^T(t-\tau)] = E\left[\left\{C^{-1}\boldsymbol{\xi}\right\}\left\{C^{-1}\boldsymbol{\xi}\right\}^T\right], \quad (4.19)$$

$$= C^{-1}E[\boldsymbol{\xi}\boldsymbol{\xi}^T]C^{-T} \quad (4.20)$$

with $C^{-T} \equiv inv(C)^T$. Thus, the noise covariance matrix of the estimated states (for the discrete model) in terms of the covariance of the optic flow estimates is given by

$$R_{\mathbf{nn}} = \frac{\Delta\gamma R_{\nu\nu}}{\pi} C^{-1}\left\{\frac{1}{\pi}\sum_{i=1}^{n}\mathbf{F}(\gamma_i)\mathbf{F}^T(\gamma_i)\Delta\gamma\right\}C^{-T}. \quad (4.21)$$

4.2 Kalman Filtering

In previous literature, authors have applied Kalman filtering to either improve optic flow estimates [29], or improve inertial state estimates from an IMU [10]; however, the thrust of this research is to apply Kalman Filtering to improve relative state estimates. Dynamically filtering the WFI outputs, opposed to raw optic flow estimates, drastically reduces computational requirements, and it allows a straight forward implementation of the Kalman filter. Figure 4.3 illustrates how a Kalman filter can be implemented for closed loop control in the WFI framework.

The Kalman filter is defined by an iterative process; first, an estimate for the initial mean and error covariance matrix are given (or assumed):

- $\hat{\mathbf{x}}_o^- = E[\mathbf{x}]$
- $P_o^- = E[(\mathbf{x_o} - \hat{\mathbf{x}}_o^-)((\mathbf{x}_o - \hat{\mathbf{x}}_o^-)^T]$

Then, for each additional time step, the following computations are repeated:

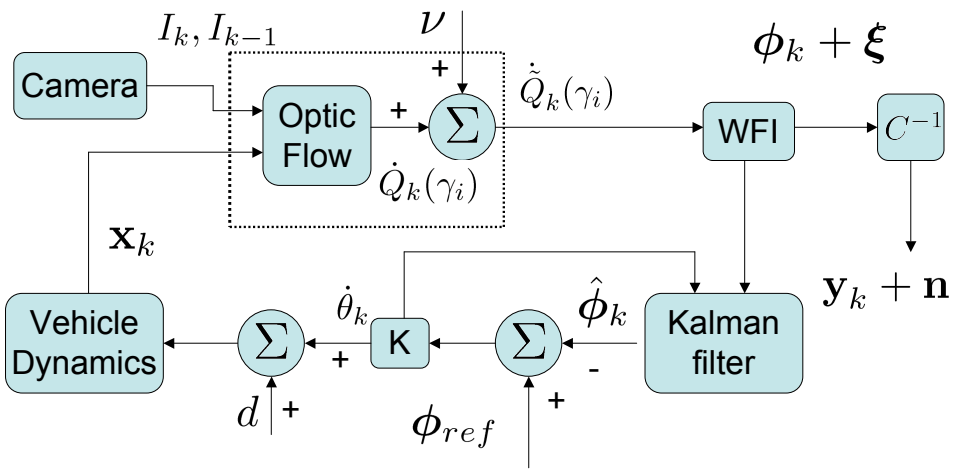

Figure 4.3: Expansion of the plant dynamics and sensing block, as it would appear in a standard unity feedback block diagram.

1. Compute the Kalman Filter gain:

   $K_k = P_k^- H_k^T (H_k P_k^- H_k^T + R_k)^{-1}$

2. Compute the current mean state estimate:

   $\hat{\mathbf{x}}_k = \hat{\mathbf{x}}_k^- + K_k(\mathbf{y_k} - H\hat{\mathbf{x}}_k^-)$

3. Compute the error covariance matrix at the current time step:

   $P_k = (I - K_k H_k) P_k^-$

4. Project the state estimate to the next time step using the model:

   $\mathbf{x}_{k+1}^- = F_k \hat{\mathbf{x}}_k + G_k \mathbf{u_k}$

5. Project the error covariance matrix based the model:

   $P_{k+1}^- = F_k P_k F_k^T + Q_k,$

   for $k = 1, 2, \cdots$,N(ΔT).

Chapter 5

Rotation Tests

The goal of the rotation tests is to gain insight into the noise characteristics of the optic flow estimates, as well as quantify how the noise varies as a function of image contrast, rotation rate, and background lighting. There are four reasons a rotation apparatus is used. First, each test run can be executed exactly the same as all the others. Second, it is easier to record longer data sets using the circular environment - opposed to the straight tunnel environment. Third, if the algorithms provide unbiased estimates, then the difference between the estimated optic flow and the true optic flow will be only noise. Fourth, the ideal optic flow depends on accurate modeling of the nearness function, however, at the beginning and end of a straight tunnel the nearness function (2.2) is not valid, but is instead modeled as $\mu = \mu_o + \Delta\mu$; thus, the residuals would have error introduced by $\Delta\mu$.

Contrastingly, there are two downsides of using the rotation apparatus. First, in the cylindrical test environment, the optic flow estimates in each cell are approximately tangent to the instantaneous velocity of the objects relative the vehicle. However, in a straight tunnel, the optic flow and the relative velocity of objects in the environment are skewed. This skewing affects the spatial frequency of the image intensity with respect to the vehicle, and undoubtedly increases the error. A second downside of using a rotation apparatus is that if the image has a localized area where

the algorithm has difficulty predicting accurate estimates, a periodic fluctuation in the optic flow signal may arise.

Figure 5.1: Nominal image for spin tests.

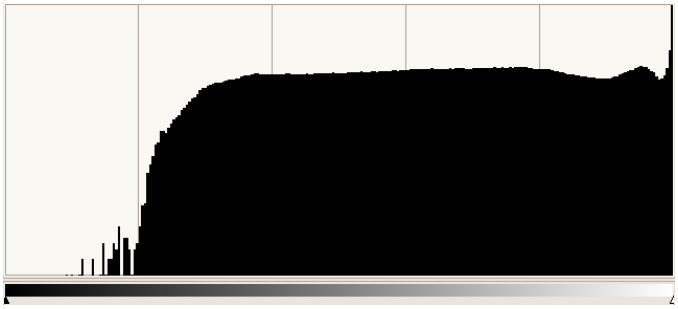

Figure 5.2: Contrast histogram for nominal Linear Park image.

The optic flow noise is analyzed with respect to the residuals, the autocorrelation, and the power spectral density (PSD). The residuals give an estimate of the optic flow variance by finding the least square error between the estimated optic flow values, and the known rotation rate:

$$\hat{R}_{\nu\nu} = \sum_{k=1}^{N} \sum_{i=1}^{n} \frac{\left[\dot{Q}_E(k,\gamma_i) - \dot{Q}_I(k,\gamma_i)\right]^2}{Nn}, \tag{5.1}$$

where $\dot{Q}_E$ and $\dot{Q}_I$ are the estimated and ideal optic flow estimates respectively, and the discrete time argument k has been incorporated in the parenthesis to clarify notation. The autocorrelation gives an estimate of how correlated the noise estimates are at different sample times. If the number of samples is large relative to the lag

time, then

$$\hat{R}_{\nu\nu}(l) = \frac{1}{N}\sum_{k=1}^{N-l}\left[\dot{Q}_E(k) - \dot{Q}_I(k)\right]\left[\dot{Q}_E(k+l) - \dot{Q}_I(k+l)\right] \tag{5.2}$$

gives an accurate estimate of the autocorrelation [19] for a given viewing angle, where l represents the lag time. The spectral density, on the other hand, analyzes the noise in the frequency domain, and is computed based on the fourier transform of the optic flow less any bias:

$$\dot{Q}^*(r) = \Delta T \sum_{k=0}^{N-1}[\dot{Q}_E(k) - \dot{Q}_I(k)]e^{-j(2\pi rk/N)}, \tag{5.3}$$

where $\dot{Q}^*(r)$ is the power of the optic flow signal at r rad/s [19].

5.1 Results

The rotation test consists of spinning the ground robot between 0.65 rad/s and 3.93 rad/s on a test stand, and recording the optic flow estimates using each algorithm. The nominal configuration refers to the Linear Park image (Figure 5.1) at the contrast level described by the histogram in Figure 5.2, and a background light intensity measured as 159 Lux (or, all the lights on in the lab). Additional tests are run to determine if varying the image contrast, or background lighting has any effect on the noise description, or variance levels.

5.1.1 Nominal Configuration

In this section, the optic flow is analyzed in order to determine first if the noise is white; second, if the optic flow and state estimates fit a Gaussian distribution;

and third, if the optic flow estimates are uncorrelated with themselves at different viewing angles. Optic flow estimates, as well as the corresponding $\dot{\theta}$ estimates based on the a_0 Fourier coefficients, are illustrated in Figure 5.3 for a rotation rate of 0.65rad/s. The empirical results are in excellent agreement with the predicted bounds, and this suggests the noise model assumptions are valid. Figure 5.4 illustrates the optic flow less the average rotation rate for one cell, as well as the corresponding autocorrelations and PSDs; again, these plots correspond to a rotation rate of 0.65rad/s. A periodic signal is clearly evident, and by comparing at what time these drops in optic flow occur with the imagery being viewed at each cell, it was determined that these drops result from a tree in Figure 5.1 that is in the shadows. These momentary drops in optic flow are most evident in the LK algorithm, and least evident in the NE algorithm. If these periodic variations are ignored, however, the noise does appear to be white. The autocorrelation and power spectral density plots also suggest the noise is white. The periodicity in the time history manifests itself in the autocorrelation function as the smaller peaks at non-zero time lags, and in the PSD plots as the higher power in the lower frequency range. At higher rotation rates, as illustrated in Figure 5.12, the noise does not appear to be white, but instead has some localized spectral content below 10Hz. At higher frequencies the noise does appear to be band-pass white, but since the Nyquist frequncy is 10Hz this result has no impact on the results.

The probability density of the optic flow and the corresponding Fourier coefficients are also of interest. Histograms representing normalized probability distributions for both of these quantities are illustrated in Figure 5.6. The optic flow is

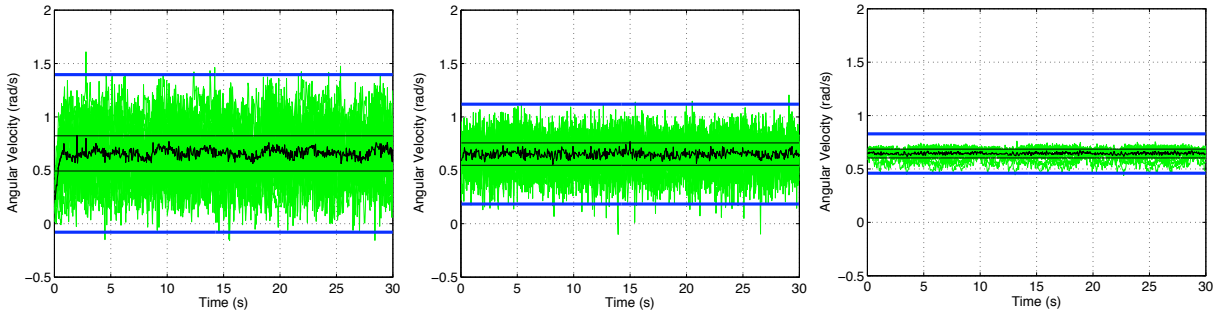

(a) NE (b) GM (c) LK

Figure 5.3: Examples optic flow and WFI $\dot{\theta}$ estimates. The theoretical 3σ bounds for $\dot{\theta}$ (black lines) are based on the derivations in Section 4, and the corresponding RMS error observed for the optic flow in that trial. The ground robot is rotating at 0.65 rad/s, with the nominal wall imagery.

most normally distributed using the GM, followed by the NE, and lastly the LK algorithm. The LK algorithm is the least normally distributed because the periodic drops in optic flow increases the number of entries in the histogram corresponding to lower speeds, relative to those corresponding to higher speeds. Since the Fourier coefficients are computed based on the summation of the estimated optic flow of each cell, the Fourier coefficients will become Gaussian as the number of cells increases as a consequence of the central limit theorem [23].

In addition to the auto-covariance, the cross-covariance of optic flow at different cells is of interest. Figure 5.7 gives examples of the cross-covariance for each algorithm, and because the magnitude of the cross-covariance is much less than the magnitude of the auto-covariance, the simplifications made in Section 4 are reasonable.

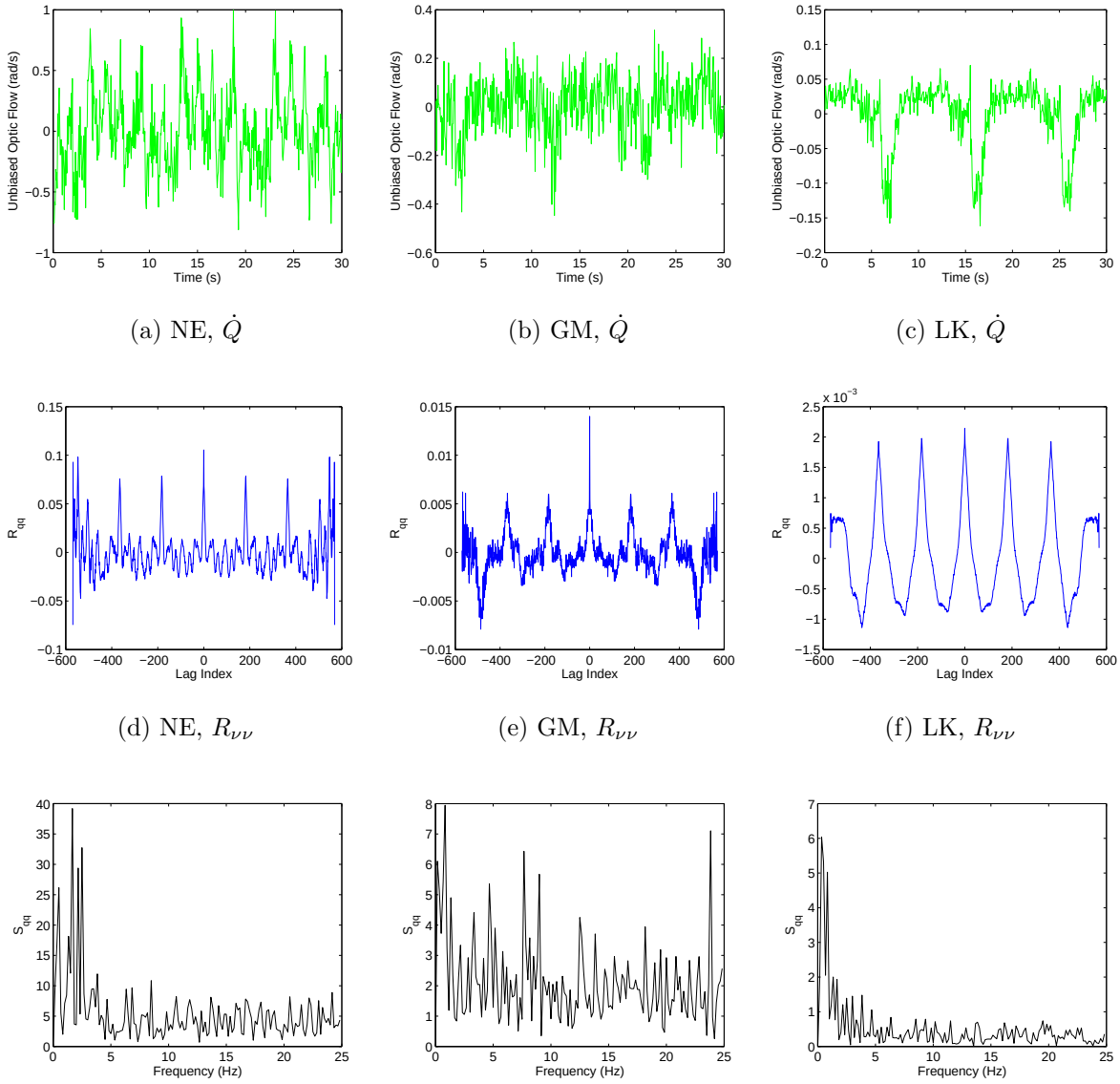

(a) NE, $\dot{Q}$ (b) GM, $\dot{Q}$ (c) LK, $\dot{Q}$

(d) NE, $R_{\nu\nu}$ (e) GM, $R_{\nu\nu}$ (f) LK, $R_{\nu\nu}$

(g) NE, PSD (h) GM, PSD (i) LK, PSD

Figure 5.4: Examples of optic flow time series, autocorrelation and power spectral densities of one cell for spinning test at 0.65 rad/s. Linear Park image with nominal configuration.

5.1.2 Off-Nominal Configurations

In this section, the covariance and spectral-density of the optic flow will be evaluated using the off-nominal contrast levels, and the off-nominal lighting condi-

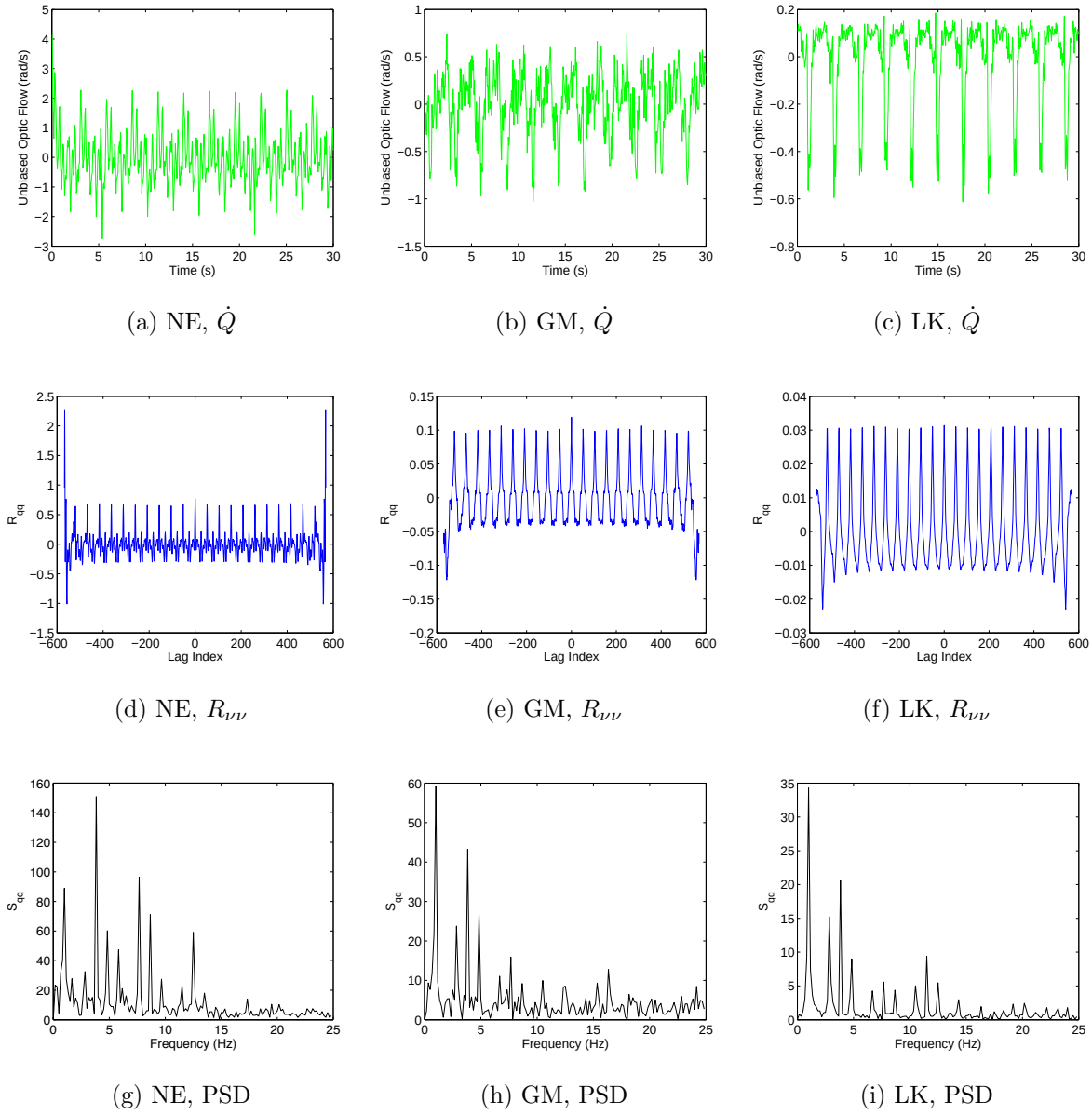

(a) NE, $\dot{Q}$ (b) GM, $\dot{Q}$ (c) LK, $\dot{Q}$

(d) NE, $R_{\nu\nu}$ (e) GM, $R_{\nu\nu}$ (f) LK, $R_{\nu\nu}$

(g) NE, PSD (h) GM, PSD (i) LK, PSD

Figure 5.5: Examples of optic flow time series, autocorrelation and power spectral densities of one cell for rotation test at 2.29 rad/s. Linear Park image with nominal configuration.

tions for the Linear Park image. The images with different contrast levels are given in Figure 5.8, while the means and standard deviations of the pixel intensities are

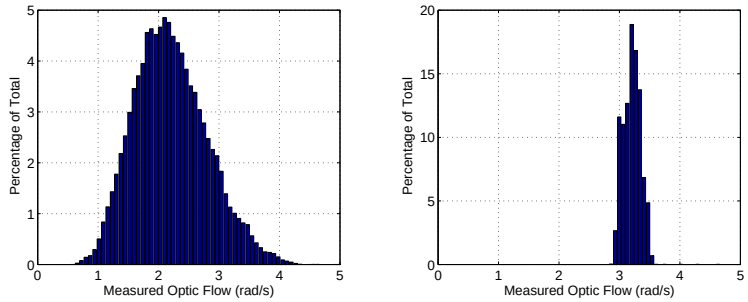

(a) NE, $\dot{Q}$

(b) NE, a_0

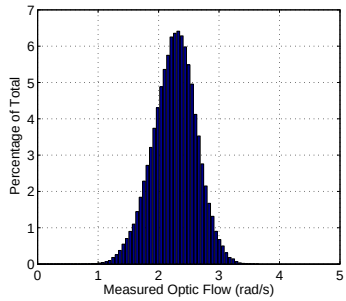

(c) GM, $\dot{Q}$

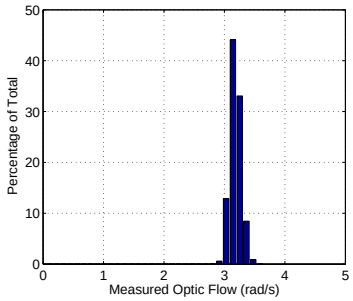

(d) GM, a_0

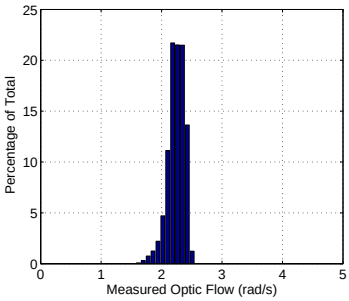

(e) LK, $\dot{Q}$

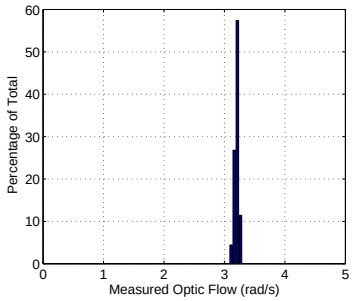

(f) LK, a_0

Figure 5.6: Experimentally determined probability distributions using 5 min of data sampled at 20Hz.

given in Table 7.1. The different lighting levels are quantified using a light meter, and are listed in Table 5.2. Lastly, another image, referred to as Tree Field, is used to to test the validity of these results. The results of the LK algorithm for

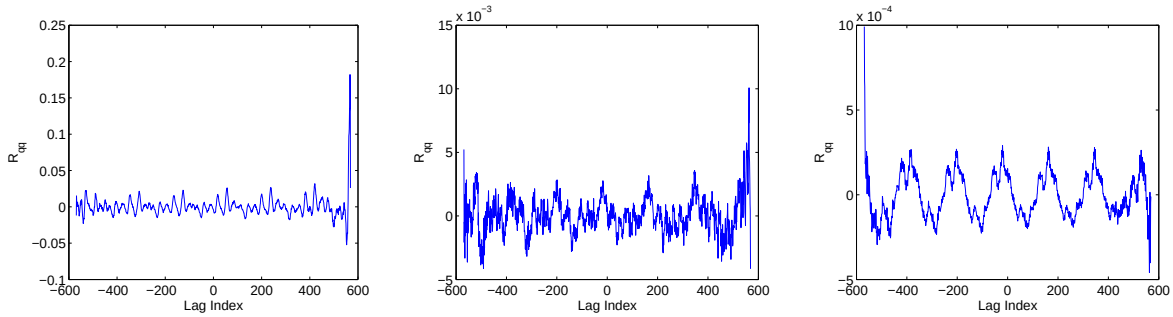

(a) NE (b) GM (c) LK

Figure 5.7: Examples of crosscorrelation plots for NE, GM, and LK at 0.65 rad/s.

Table 5.1: Contrast levels for each Linear Park image.

Image	Mean Intensity (0-255)	Std. Dev.
LP 100 (nominal)	175	54.6
LP 60	175	32
LP 40	174	22

decreased contrast levels in the panorama are given in Figure 5.10. Decreasing the contrast levels does not have a noticeable effect on the noise characteristics, except to possibly increase the magnitude of the variance; however, this effect is explored in the next section. On the other hand, the results of the LK algorithm for decreased background lighting are given in Figure 5.9. These plots show that the time history, autocorrelation and PSD at lower light levels no longer exhibit the dominant low frequency component observed in the nominal configuration. The affect of low lighting conditions on optic flow estimates are explored more in [4]; however, the

(a) Linear Park, 60% contrast level

(b) Linear Park, 40% contrast level

(c) Tree Field

Figure 5.8: Off-nominal panoramas.

conclusions reached are inline with these results, in that as the light decreases, so to does the effectiveness of estimating relative state information using optic flow. Lastly, the results for the LK algorithm using the Tree Field image are given in Figure 5.11. These results are similar to those of the nominal Linear Park image.

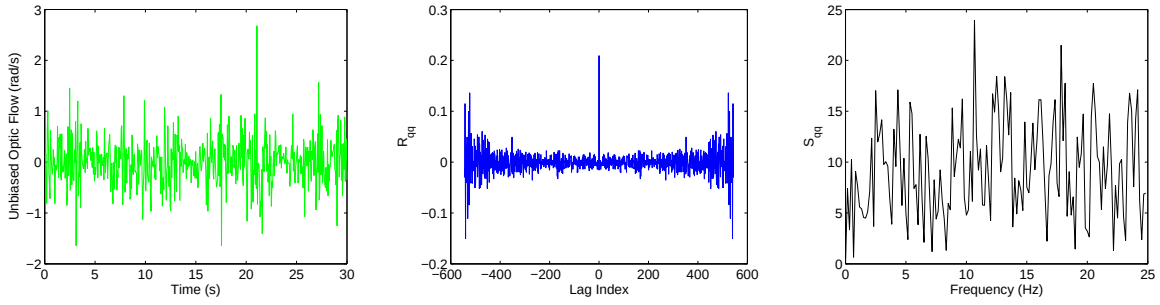

(a) Optic flow (b) Auto-covariance (c) Power spectral density

Figure 5.9: Examples of LK optic flow time series, autocorrelation and power spectral densities of one cell for rotation test at 0.65 rad/s. Linear Park image with low lighting.

Table 5.2: Background luminosity levels.

Lighting Condition	Lux
Full	159
Medium	65
Low	5.3

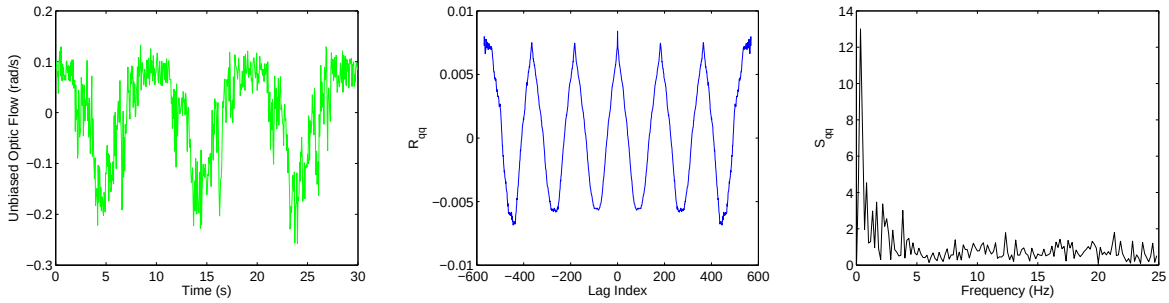

(a) Optic flow (b) Auto-covariance (c) Power spectral density

Figure 5.10: Examples of LK optic flow time series, autocorrelation and power spectral densities of one cell for rotation test at 0.65 rad/s. Linear Park image with 40% contrast.

5.1.3 Quantifying Optic Flow Variance as a Function of Rotation Rate

For each condition previously described, the variance of the optic flow - as well as any bias - is analyzed in this section as a function of the vehicle's rotation rate. The variance in these plots was computed based on (6.4). It was found that

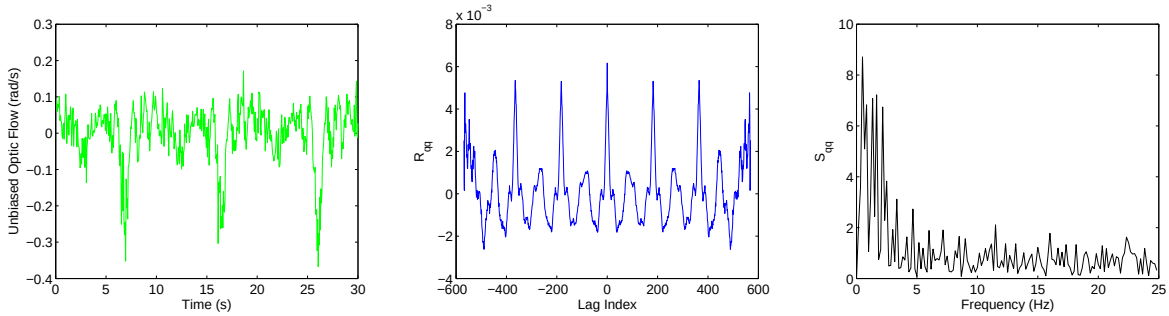

(a) Optic flow (b) Auto-covariance (c) Power spectral density

Figure 5.11: Examples of LK optic flow time series, autocorrelation and power spectral densities of one cell for rotation test at 0.65 rad/s. Tree Field imagery.

the LK algorithm yields the least amount of variance, while the NE algorithm has the most amount of variance. Furthermore, with the exception of the estimates made with low lighting, this variance increases in a nearly perfect quadratic trend for the LK and GM algorithms, and an exponential trend for the NE algorithm, as quantified by every trial having a 98% or better correlation with the corresponding trend curve.[1] The results from the Tree Field imagery are in agreement with results from the Linear Park image.

Bias in the optic flow estimates can be quantified as either local - corresponding to the optic flow estimates in individual cells, or as global - corresponding to the over (or under) average optic flow estimate over all the cells. The local bias can be investigated by plotting the optic flow as a function of the viewing angle at a given time. As illustrated in Figure 5.13, there is local bias, and it is the result of the parabolic mirror being offset from the camera. A global optic flow bias can

[1]The NE algorithm at 40% contrast fit this description using a quadratic trend curve.

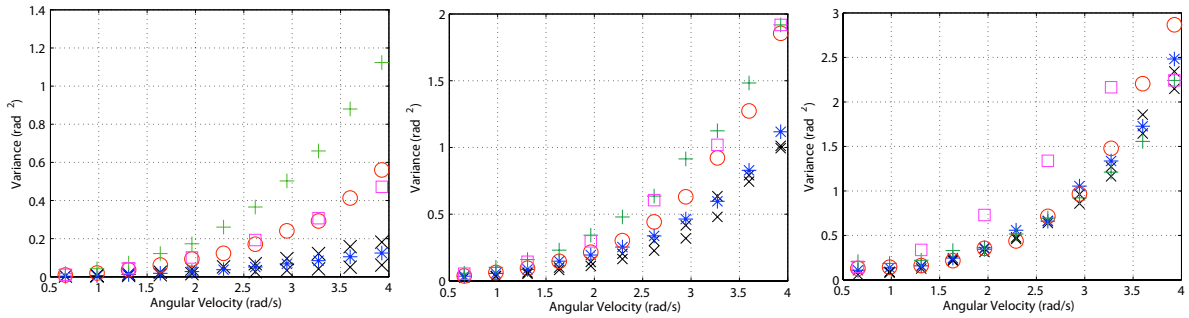

(a) LK, without low light (b) GM, without low light (c) NE, without low light

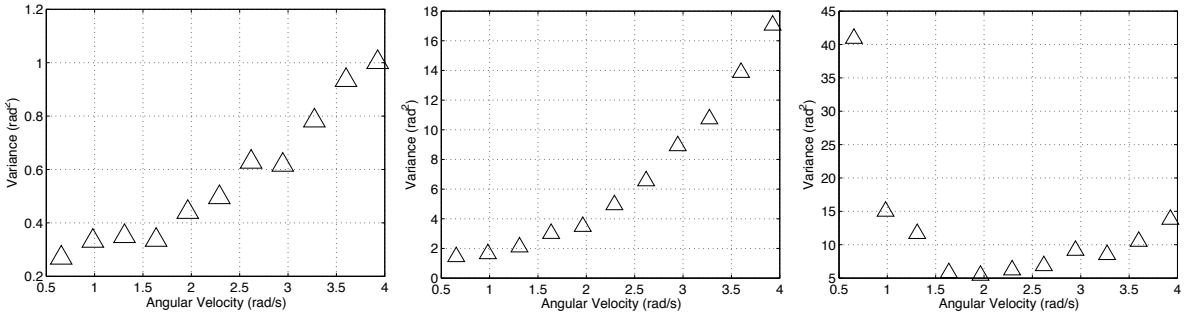

(d) LK, low light (e) GM, low light (f) NE, low light

Figure 5.12: Optic flow variance as a function of vehicle rotation rate. 'x' = nominal configuration, '*'= medium lighting, 'o'=60% contrast, '+' = 40% contrast,square = Tree Park, and triangle = low lighting.

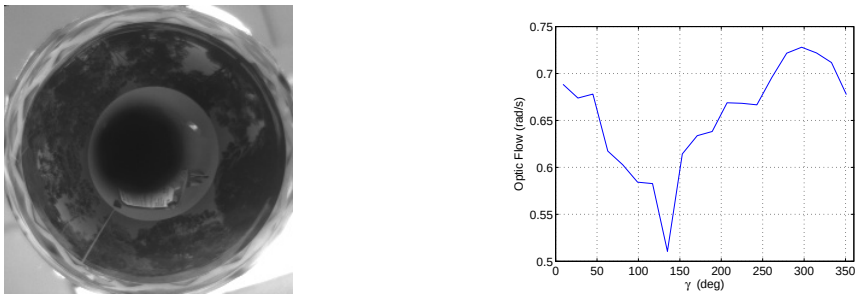

(a) Camera offset (b) LK, Optic flow

Figure 5.13: Illustration of the cause (a) and effect (b) of the local bias.

be investigated by comparing the average optic flow estimate at each viewing angle with the known rotation rate. Figure 5.14 plots the required scaling factor for the optic flow estimates to be converted from pixels/frame (which is what the individual algorithms estimate) to rad/s in order to provide an unbiased estimate. The LK algorithm has a conversion factor that is nearly constant across all rates. The GM is approximately constant at lower turn rates, however, it steadily increases at rotation rates greater than 1.5 rad/s for all. The NE algorithm's conversion factor is roughly quadratic with angular velocity. In addition, the magnitude for the conversion factor changes drastically for the trials with low light. It should be noted, however, that the theoretical conversion factor is 0.1428, which is close to the conversion factor experimentally determined for the LK algorithm. The theoretical conversion factor is determined based on the number of metapixel that are in each row of the image, the overall width of the image, and the framerate.

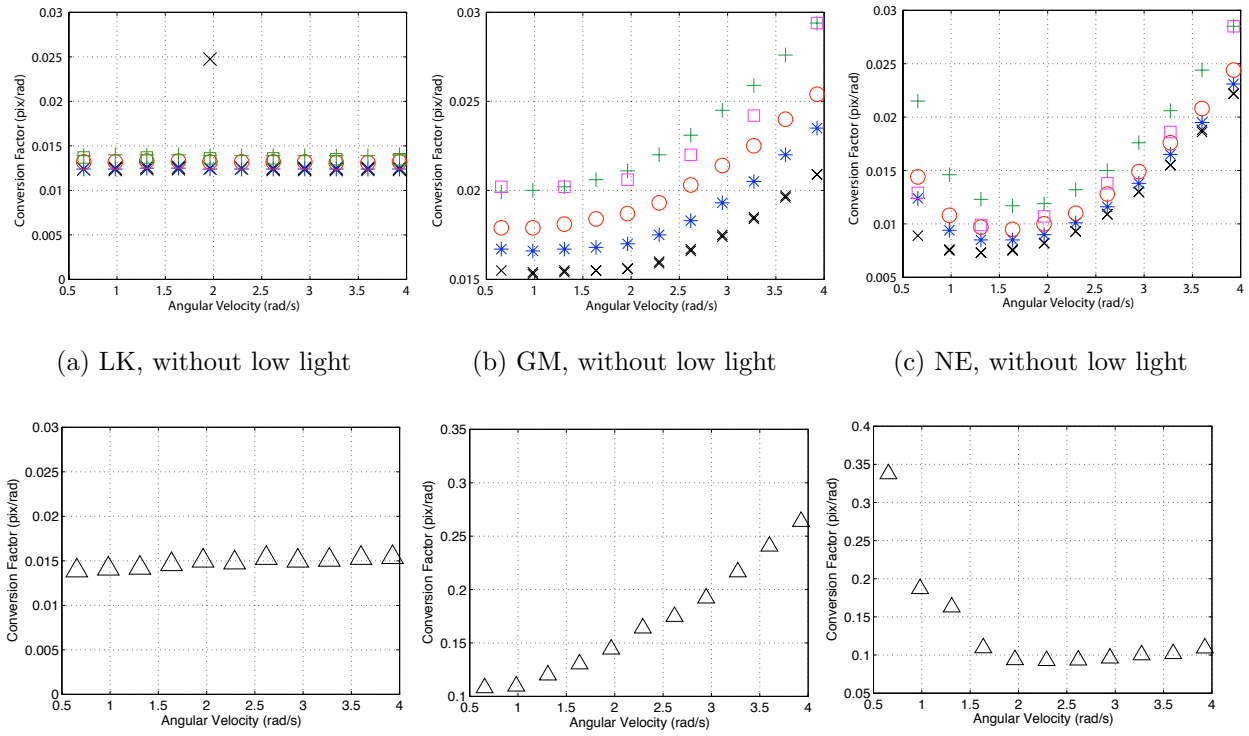

(a) LK, without low light (b) GM, without low light (c) NE, without low light

(d) LK, low light (e) GM, low light (f) NE, low light

Figure 5.14: Optic flow conversion factor as a function of vehicle rotation rate. 'x' = nominal configuration, '*'= medium lighting, 'o'=60% contrast, '+' = 40% contrast,square = Tree Park, and triangle = low lighting.

Chapter 6

Straight Tunnel Tests

The ground robot, whose dynamic model was described in Section 3, is a useful tool in evaluating the performance of different optic flow algorithms in closed loop. To quantify the ground robot's ability to track the centerline of a tunnel given an initial offset, the GM, LK and NE algorithms were implemented in the WFI framework with proportional feedback on the a_1 and a_2 Fourier coefficients. The forward velocity was held constant using an inner loop feedback controler designed by the manufacturer. In addition, there were 20 tests conducted with an initial 25 cm lateral offset, and 20 tests with an initial 45° orientational offset. The Vicon System simultaneously measured the true position and orientation of the robot at 350 Hz.

6.1 Ground Robot Experimental Setup

The ground robot is a Dr. Robot X80 model. This configuration includes the company's standard chassis, wheel motors and motor control. In addition, the onboard computer has a VIA motherboard and AMD Sempron 3400+ processor with a clock frequency of 2.0 GHz. The L1 and L2 caches are 128 and 256Kb respectively, the front side bus frequency is 200MHz, and there is 1Gb of ram. The computer interfaces with a FireWire camera, processes the imagery, and uses a serial

port to send motor commands at 20 Hz. To obtain a 360° field of view, the camera points upward into a panoramic mirror installed above the robot.

6.2 Performance Comparison Metrics

The results are analyzed with respect to two key metrics. First, how well the optic flow estimates made by each algorithm compare with the ideal optic flow values- which are reconstructed offline based on (2.1) using the Vicon state-measurements. Second, how well the robot is able to track the tunnel centerline using each algorithm. The first metric evaluates the three algorithms purely in terms of computational accuracy, while the second metric evaluates each algorithm in regards to closed-loop performance.

These metrics are quantified first in terms of the RMS error and second in terms of the mutual information between the ideal and measured optic flow - as well as between the true and estimated states. The RMS error between two data sets $\{\alpha_i\}_{i=1}^N$ and $\{\beta_i\}_{i=1}^N$ is defined as

$$RMS(\alpha, \beta) = \sqrt{\frac{\sum_{i=1}^N (\alpha_i - \beta_i)^2}{N}}. \tag{6.1}$$

Mutual information provides a statistical benchmark to evaluate how well knowledge of one random variable represents knowledge of another. However, unlike a correlation coefficient - which detects only linear dependance between two stochastic processes - the mutual information detects any dependance, and is invari-

able through linear transforms [11]. It can be defined as

$$MI(\alpha,\beta) = \sum_{\alpha}\sum_{\beta} p(\alpha,\beta)\log_2 \frac{p(\alpha,\beta)}{p(\alpha)p(\beta)}, \tag{6.2}$$

where $p(\alpha)$ and $p(\beta)$ are the marginal probabilities for the data sets $\{\alpha_i\}_{i=1}^{N}$ and $\{\beta_i\}_{i=1}^{N}$, and $p(\alpha,\beta)$ is the joint probability between the data sets. The log function is chosen to have base 2 so that the mutual information is in units of bits [25]. In general, if α and β are uncorrelated random variables, then the mutual information between the two is zero; the more correlated these data sets are, however, the greater the mutual information. Furthermore, since the marginal and joint probability functions are not known, these quantities are estimated by constructing a joint histogram. The number of bins in the joint histogram is chosen based on experimentally determining how many bins can be included until the mutual information begins to increase precipitously [11]. As the number of bins in the joint histogram is increased, the mutual information should increase until it reaches a steady state value [26] and [24]; however, as discussed in [11] and [26], an overestimate of the mutual information occurs from over-binning. Although there are several methods to compensating for this bias [9], an interpolation between the bias estimate discussed in [11] and a heuristic model based on the number of bins in the joint histogram [26] was implemented. This interpolation is necessary because it was experimentally found that the adjustment recommended in [11] underestimates this bias, while the heuristic method overestimates it. Interpolating between these two estimates was recommended in [26]. This method determines a scaling factor so the linear combination of the two bias estimates result in a constant value of mutual information

for two different bin sizes after the precipitous increase in mutual information has begun. In other words, given an estimate of the mutual information and the two bias' corresponding to N_i bins, the true mutual information can be can be computed as

$$MI_T(N_i) \quad = \quad MI_E(N_i) - \alpha BIAS_1(N_i) - (1-\alpha)BIAS_2(N_i), \tag{6.3}$$

where the subscripts T and E correspond to the true and estimated mutual information, and α is chosen so that MI_T is equal for N_i and N_{i+1}. Furthermore, the resolution of the bins is defined to be finest around values that are most frequently observed, and the broadest around the values that are least frequently observed [26].

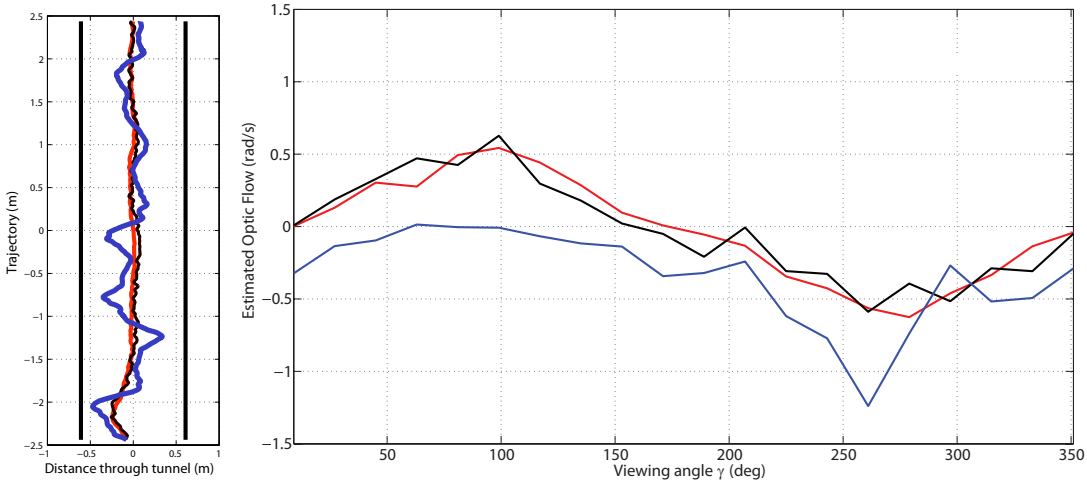

(a) Average Trajectories

(b) Example optic flow function

Figure 6.1: Average robot measured trajectories, and example optic flow function at 80% down the tunnel. Red = LK, Black = GM, Blue = NE.

6.3 Results

The LK algorithm generally yields the best performance, followed by the GM, and lastly the NE. These result are quantified by lower RMS error, and higher mutual information - as listed in Tables 6.1 and 6.2. The performance of the robot can be improved by optimizing the gains individually for each algorithm; but, in the current framework the gain selection is limited by the performance of the NE algorithm. For instance, the robot in the NE trials had a tendency to overshoot - both in position and orientation; however, using lower gains meant that it could not react to the initial orientation offset in time to avoid the wall. With these constraints in mind, the NE algorithm is still able to successfully negotiate the tunnel.

The plots representing mutual information (Figure 6.4) as a function of the histogram bin size includes the two bias estimates. In these figures, $BIAS_2$ clearly underestimates the true bias, while $BIAS_1$ is the heuristically model and noticeably over-estimates the true bias.

The affect that the optic flow bias previously discussed in reference to the rotation tests can also be analyzed based on the residuals between the estimated and ideal optic flow for the straight tunnel environment. This error is found by computing

$$\hat{R}_{\nu\nu} = \sum_{run=1}^{20} \sum_{k=1}^{N} \frac{\left[\dot{Q}_E(k, run) - \dot{Q}_I(k, run)\right]^2}{20N}. \tag{6.4}$$

Figure 6.5 illustrates this variance as a function of γ for each algorithm. Since the ground robot mostly followed a straight line, the magnitude of the optic flow was largest at 90° and 270°; therefore, the uncertainty is greatest in these regions. The

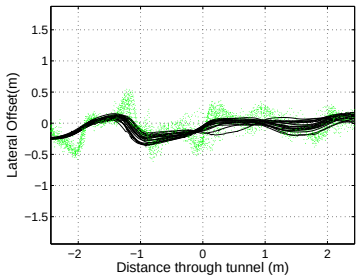

(a) NE, lateral offset

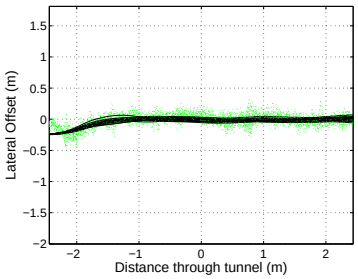

(b) GM, lateral offset

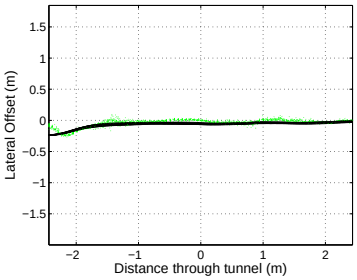

(c) LK, lateral offset

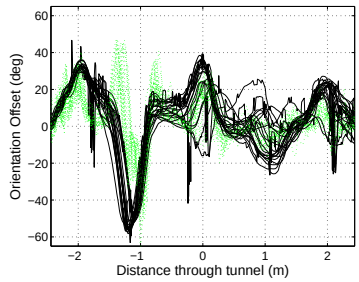

(d) NE, angular deviation

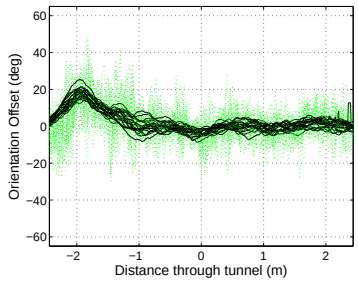

(e) GM, angular deviation

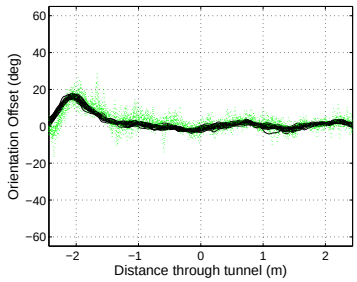

(f) LK angular deviation

Figure 6.2: Trajectories and angular perturbations from the centerline for each algorithm given an initial 25cm lateral offset. Black lines = Vicon measured states, Green lines = WFI state estimates.

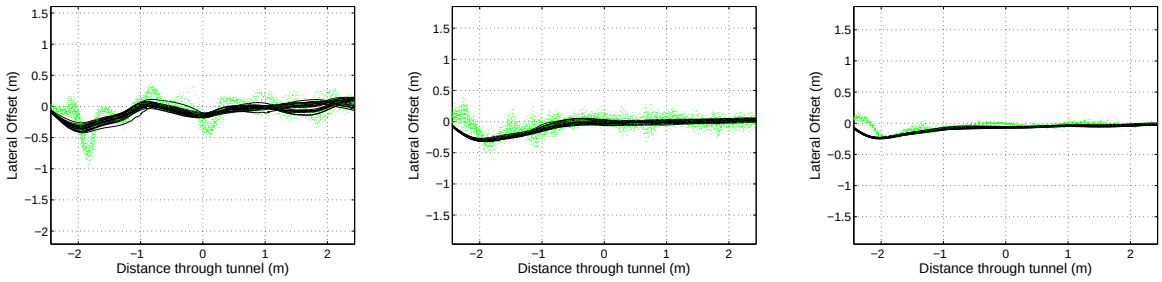

(a) NE, lateral offset (b) GM, lateral offset (c) LK, lateral offset

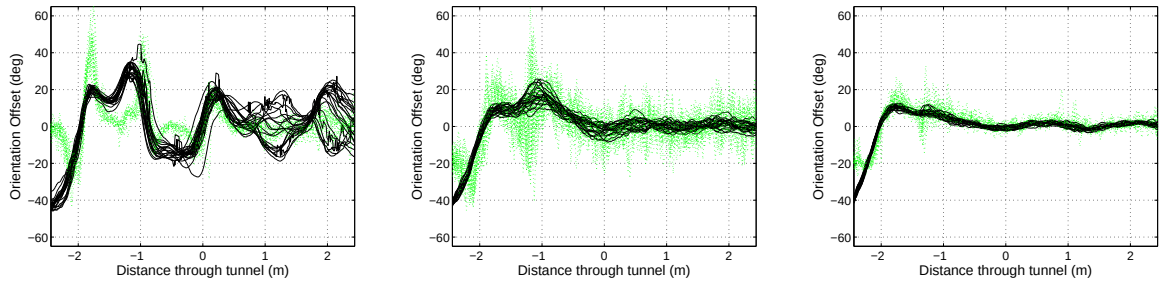

(d) NE, angular deviation (e) GM, angular deviation (f) LK angular deviation

Figure 6.3: Trajectories and angular perturbations for each algorithm given an initial 45° offset. Black lines = Vicon measured states, Green lines = WFI state estimates.

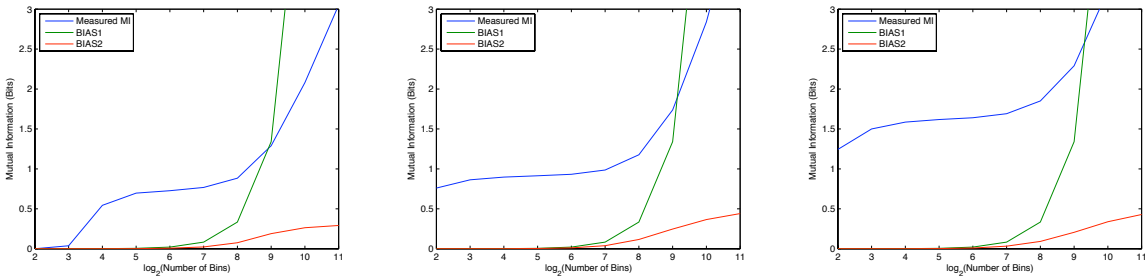

(a) NE (b) GM (c) LK

Figure 6.4: Mutual information between measured and ideal optic flow, as well as both bias estimates

Table 6.1: RMS error for optic flow, trajectory and orientation, based on straight tunnel environment.

RMS Error	Initial Lateral Offset			Initial Orienation Offset		
	NE	GM	LK	NE	GM	LK
True Trajectory vs centerline (mm)	131	75	82	144	130	105
True Trajectory Standard Deviation (mm)	49	23	8	42	22	9
Estimated vs True Trajectory (mm)	142	78	43	143	110	70
Estimated vs Ideal Optic Flow (rad/s)	10.3	1.2	0.8	6.7	1.2	0.7
Estimated vs True Orientation (deg)	16	8	3	14	9	4
Test Standard Error (mm)	11	5	2	10	5	2

Table 6.2: Mutual Information for optic flow, trajectory and orientation, for straight tunnel environment.

Mutual Information (bits)	Initial Lateral Offset			Initial Orienation Offset		
	NE	GM	LK	NE	GM	LK
Estimated vs Ideal Optic Flow	0.70	0.98	1.76	0.72	0.95	1.67
Estimated vs True Trajectory	0.58	0.89	1.05	0.85	0.64	1.14
Estimated vs True Orientation	0.79	0.37	0.78	0.81	0.70	1.19

unequal magnitudes of these variances at 90° and 270°, however, is the result of the local bias of the optic flow estimates as described in Section 5.1.3.

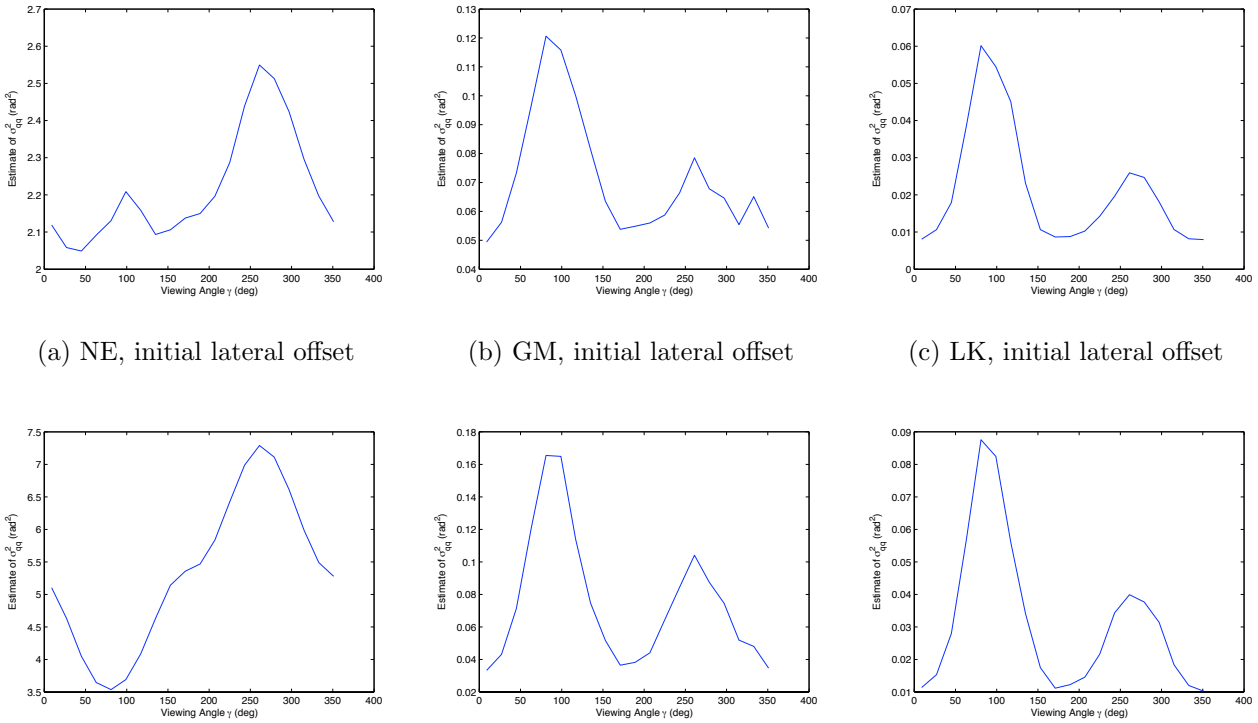

(a) NE, initial lateral offset (b) GM, initial lateral offset (c) LK, initial lateral offset

(d) NE, initial angular deviation (e) GM, initial angular deviation (f) LK, initial angular deviation

Figure 6.5: Estimate of the variance for each algorithm based on residuals, assuming white noise

Chapter 7

Kalman Filtering in Closed Loop

A discrete Kalman filter was implemented using the frame work developed in Section 4.2, based on the discrete model of the ground robot from Section 3. The impact that the Kalman filter has on the performance of the ground robot is quantified by comparing the Vicon measured states with both the Kalman filtered states, and the raw WFI states. Data was collected for the GM and LK algorithms over 20 trials in a straight tunnel with an initial lateral offset of 25cm. Results for the NE algorithm were not collected due to its inability to track the tunnel centerline. As illustrated in Figure 7.1 and Figure 7.3, the Kalman filter is very capable of removing noise from the state estimates; however, this does not guarantee that the Kalman filtered states will track the true states. In fact, the results suggest that possibly too much noise was included in the dynamic model, and it may have been beneficial to rely more on the sensor measurements than was done in these trials. The amplitude of the variance implemented in the Kalman filter was based on a manually iterative process that started with the noise estimates found in Chapter 5, and converged to a value that resulted in smooth, unbiased estimates based on running the filter offline using imagery collected from previous straight tunnel tests. The fact that the actual noise measurements for the WFI outputs are greater than the noise values predicted, supports the notion that some of the noise develops

due to the translational velocity of the ground robot. Although the LK algorithm performed consistently well in these trials, the GM had a tendency to either track the centerline very well, or largely overshoot it and continue to oscillate from one end of the tunnel to the other. It is believed that this effect could be mitigated by either optimizing the feedback gains, or modifying the noise model implemented in the Kalman filter.

Table 7.1: RMS error between raw both WFI state estimates and Kalman filtered state estimates with the Vicon measured state estimates.

Algorithm	θ (deg)	$\theta_{Kf}(deg)$	y (mm)	$y_{Kf}(mm)$
GM	19	19	163	109
LK	13	13	109	78

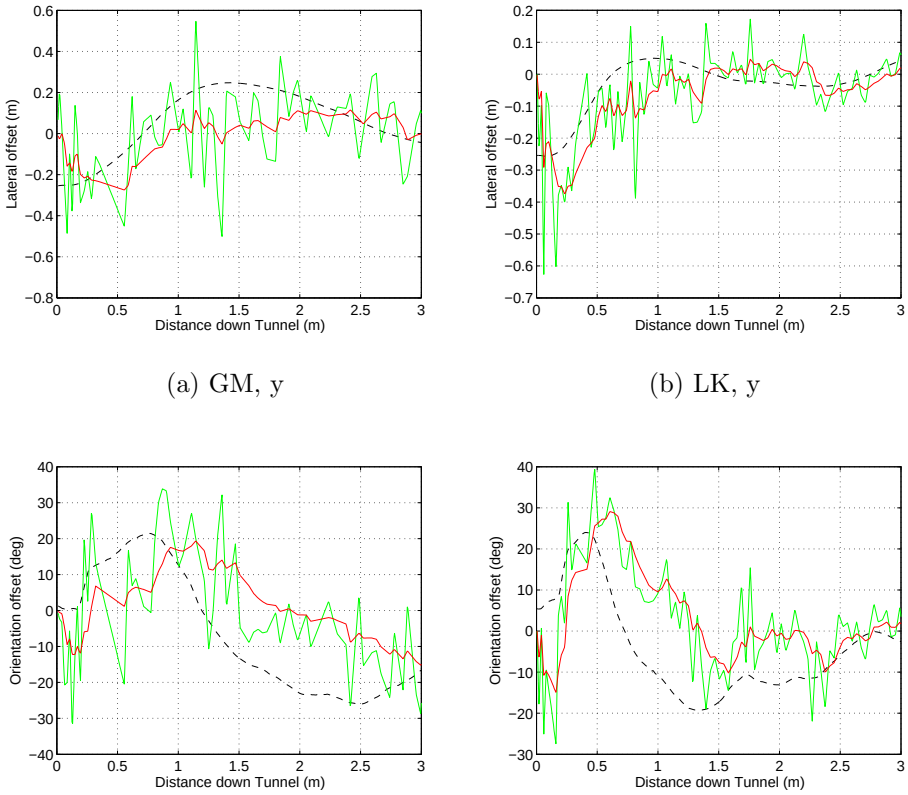

(a) GM, y

(b) LK, y

(c) GM, θ

(d) LK, θ

Figure 7.1: Example trajectories and angular perturbations from the centerline for the ground robot in a straight tunnel environment using Kalman filtered Fourier coefficients for feedback. The black dashed lines are the Vicon measurements, the green lines are the WFI state estimates, and the red lines are the Kalman filtered state estimates.

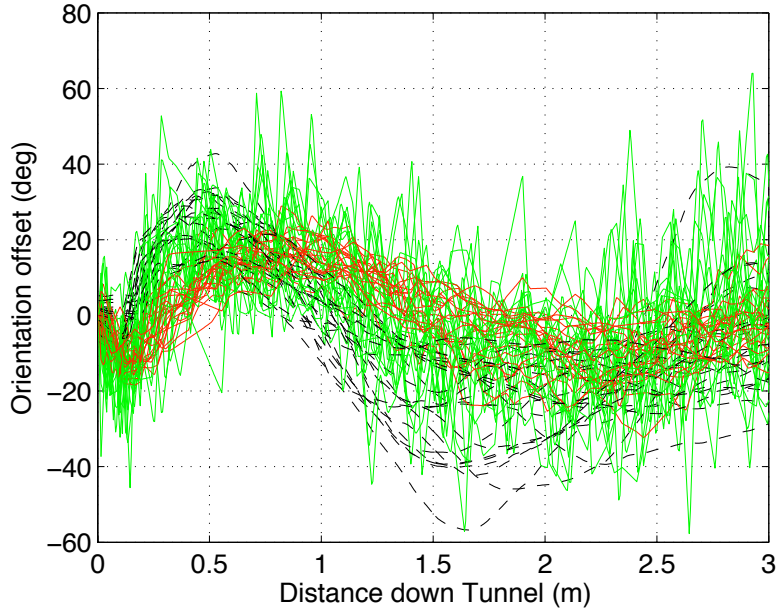

(a) θ estimate

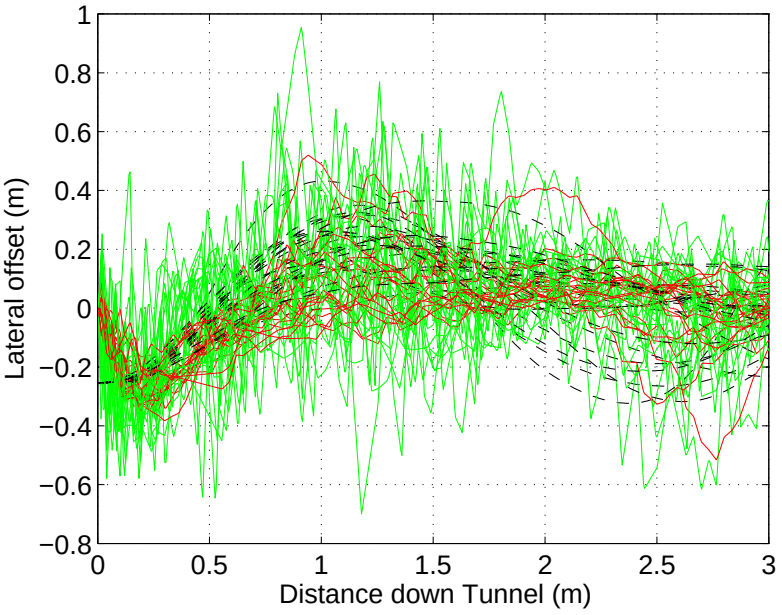

(b) y estimate

Figure 7.2: All trajectories and angular perturbations from centerline for the GM using Kalman filtered states for feedback. The black dashed lines are the Vicon measurements, the green lines are the WFI state estimates, and the red lines are the Kalman filtered state estimates.

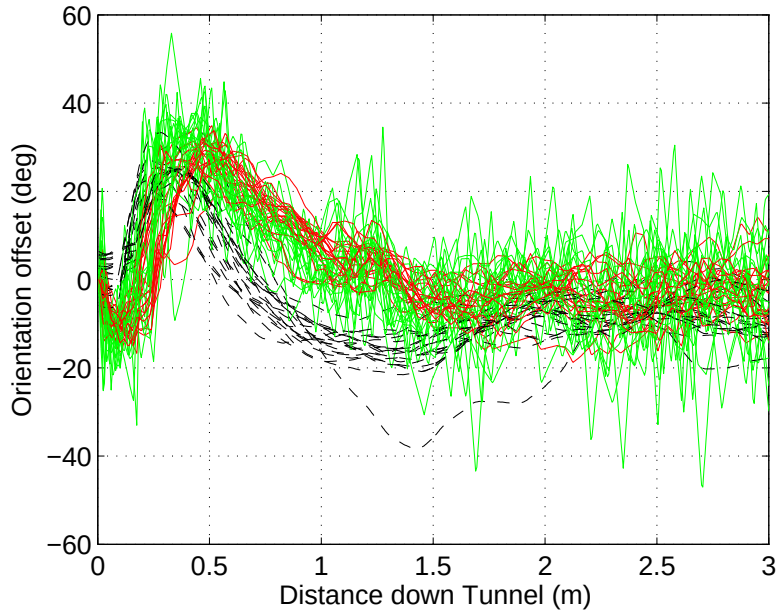

(a) θ estimate

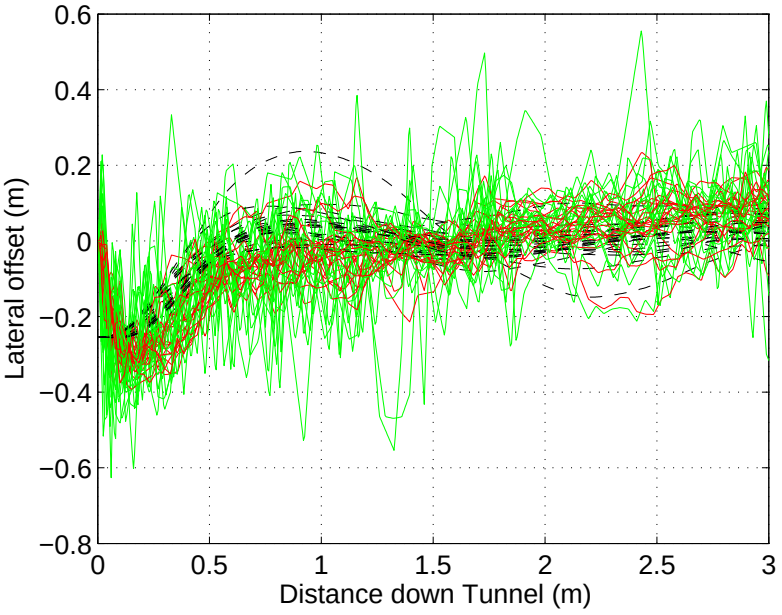

(b) y estimate

Figure 7.3: All trajectories and angular perturbations from centerline for the LK using Kalman filtered states for feedback. The black dashed lines are the Vicon measurements, the green lines are the WFI state estimates, and the red lines are the Kalman filtered state estimates.

Chapter 8

Conclusions and Recommendations for Future Work

There are several conclusions that can be made from the experiments and theory developed in this thesis. The rotation tests gave insight into the noise characteristics of the optic flow estimates, and from this it was found that these estimates are corrupted by approximately unbiased white noise when the magnitude of the optic flow estimates are low; however, as the magnitude of the optic flow was increased, the noise characteristics became colored. This coloring effect can be supported by the notion that when the true optic flow is large relative to the spatial frequency of the image, additional uncertainty is introduced into the optic flow estimate [28]. Additionally, as observed in the Kalman filtering trials, the noise estimates from the rotation tests underestimate the noise estimates in the straight tunnel. The rotation tests also analyzed the effect on optic flow with regards to low lighting, and the results support the conclusions reached in [4]; however, it is interesting to note how robust to lighting changes the LK algorithm is. The magnitude of the optic flow estimates using the NE and GM algorithms decreased considerably in low lighting conditions, while the LK algorithm was still able to provide an unbiased estimate, with only a slight increase in the variance. Lastly, the theoretic results developed a method of propagating optic flow covariance estimates to WFI output estimates. The results imply that the more sensors used, the less noisy the corre-

sponding WFI outputs will be. This conclusion is inline with the architecture of the insect visuomotor system, which relies on many simple noisy sensors to extract meaningful state information. However, this push for more sensors is contrasted with the need to have sensors spaced wide enough so that the distance a pixel shifts between frames is still detectable by the optic flow algorithm.

The straight tunnel tests compared the performance of a ground robot using three different optic flow algorithms. It was found that the LK algorithm yields the best performance, while the NE algorithm yields the worst performance; however, all algorithms were able to provide closed loop control and tunnel centering capabilities when implemented in the WFI framework. Furthermore, although the NE algorithm performed worst, it can be implemented on analogue circuitry which is very practical considering the lower power requirement for analogue VLSI chips, and the potential for applying this technology on MAV platforms. The results from the straight tunnel tests were analyzed with respect to the RMS error, as well as the mutual information between the ideal and estimated optic flow and state estimates. However, the mutual information results do not always support the conclusion that the LK algorithm performed much better than the NE algorithm. For this reason, although mutual information provides an insightful method to compare data series, it does not necessarily yield practical information regarding the performance capabilities of each algorithm.

Finally, a Kalman filter was applied to the WFI outputs in order to improve the relative state information extracted from optic flow estimates. The results yield a mixed review of the modified performance of the ground robot. On one hand, the

Kalman filter is able to drastically reduce the high frequency content in the optic flow estimates; on the other hand, these smoother results do not necessarily correlate to improved ground robot performance. Thus, in future work it will be important to investigate the effect of different noise levels, or possibly different controller gains, and how these impact the closed loop performance of the ground robot when utilizing a Kalman filter. Additionally, the local bias observed in the optic flow estimates were not taken into consideration in the filtering process. Therefore, in future work it would also be of interest to model this bias as a filter state, and compare the performance.

Bibliography

[1] J.L. Barron, Fleet D.J, and S.S. Beauchemin. Performance of optical flow techniques. *International Journal of Computer Vision*, 1994.

[2] Jean Y. Bouguet. Pyramidal implementation of the Lucas-Kanade feature tracker: Description of the algorithm, 2002. Posted at 2007-11-26 15:56:14.

[3] Robert G. Brown and Patrick Y.C. Hwang. *Introduction to Random Signals and Applied Kalman Filtering*. John Wiley and Sons, New York, 1997.

[4] Mike Chin. A comparison of optic flow in the visible light and infrared spectrum. Master's thesis, University of Maryland, 2008.

[5] John L. Crassidis and John L. Junkins. *Optimal Estimation of Dynamic Systems*. Chapman nand Hall/CRC, Washington D.C., 2008.

[6] Christopher Drew. Drones are weapons of choice in fighting Al Qaeda. *New York Times*, March 16, 2009.

[7] Martin Egelhaaf and *et al.* Neural encoding of behaviorally relevant visual-motion information in the fly. *TRENDS in Neurosciences*, 25(2):96–102, February 2002.

[8] Arthur Gelb. *Applied Optimal Estimation*. MIT press, Cambridge, MA, 1974.

[9] Peter Grassberger. Entropy estimates from insufficient samplings. eprint arXiv:physics/0307138.

[10] Pini Gurfil and Hector. Rotstein. Partial aircraft state estimation from visual motion using the subspace constraints approach. *Journal of Guidance, Control, and Dynamics*, 24(5):1016–1028, 2001.

[11] Hanspeter Herzel and Ivo Groβe. Measuring correlations in symbol sequences. *Physica A*, 216:518–542, February 1995.

[12] Berthold K.P. Horn and Brian G. Schunck. Determining optical flow. *Artificial Intelligence*, pages 185–203, 1981.

[13] J Sean Humbert and Andrew Hyslop. Bio-inspired visuometor convergence. Submitted to IEEE Transaction on Robotics June 2008.

[14] J Sean Humbert, Andrew Hyslop, and Michael Chinn. Experimental validation of wide-field integration methods for autonomous navigation. In *International Conference on Intelligent Robots and Systems*, 2007.

[15] Andrew Hyslop and J Sean Humbert. A new pixel-matching optic flow algorithm for obstacle avoidance applications.

[16] Andrew M. Hyslop and J. S. Humbert. Wide-field integration methods for autonomous navigation of 3-D environments. In *AIAA Guidance, Navigation and Control*, August 2008.

[17] R.E. Kalman. A new approach to linear filteing and prediction problems. *Transactions of the ASMEJournal of Basic Engineering*, pages 35–45, March 1960.

[18] Joseph K. Kearney, William B Thompson, and Daniel L Boley. Optical flow estimation: An error analysis of gradient-based methods with local optimization. *Pattern Analysis and Machine Intelligence*, 1987.

[19] Vladislav Klein and Eugene A. Morelli. *Aircraft System Identification, Theory and Practice*. American Institute of Aeronautics and Astronautics, Reston, Virginia, 2006.

[20] Bruce D. Lucas and Takeo Kanade. An interative image registration technique with an application to stereo vision. In *Proc. of the 7th International Converence of Artificial Inteligence*, pages 674–679, 1981.

[21] Chris McCarthy and Nick Barnes. Performance of temporal filters for optical flow estimation in mobile robot corridor centring and visual odometry. In *Australasian Conference on Robotics and Automation*, 2003.

[22] Chris McCarthy and Nick Barnes. Performance of optical flow techniques for indoor navigation with a mobile robot. In *International Conference on Robotics and Automation*, 2004.

[23] Rob Sanner. Class notes for ENAE 788K, fall 2008.

[24] A. O. Schmitt, H Herzel, and W. Ebeling. A new method to calculate higher-order entropies from finite samples. *Europhysics Letters*, pages 303–309, 1993.

[25] C.E. Shannon. A mathmatical theory of communication. *Bell System Technical Journal*, 1948.

[26] Pat Shoemaker. Email communication.

[27] Patrick A. Shoemaker and O'Carroll David C. Insect-based visual motion detection with contrast adaptation. In *Defense and Security Symposium, Infrared Technology and Applications Conference*, 2005.

[28] Eero .P. Simoncelli, Edward A. Adelson, and David J. Heeger. Probability distributions of optic flow. In *Conference on Computer Vision and Pattern Recognition*, 1991.

[29] Ajit Singh. *Optic Flow Computation: A Unified Perspective*. IEEE Computer Society Press, Los Alamitos, CA, 1991.

[30] Jan P.H. van Santen and George Sperling. Elaborated reichardt detectors. *Optical Society*, 1985.